

To build the LPBF
Simulation

Thermal Modeling in Metal Additive Manufacturing Using Graph Theory

M. Reza Yavari

Department of Mechanical and Materials
Engineering,
University of Nebraska-Lincoln,
Lincoln, NE 68588-0526
e-mail: mrezayavari89@huskers.unl.edu

Kevin D. Cole

Department of Mechanical and Materials
Engineering,
University of Nebraska-Lincoln,
Lincoln, NE 68588-0526
e-mail: kcole1@unl.edu

Prahalada Rao¹

Department of Mechanical and Materials
Engineering,
University of Nebraska-Lincoln,
Lincoln, NE 68588-0526
e-mail: rao@unl.edu

The goal of this work is to predict the effect of part geometry and process parameters on the instantaneous spatiotemporal distribution of temperature, also called the thermal field or temperature history, in metal parts as they are being built layer-by-layer using additive manufacturing (AM) processes. In pursuit of this goal, the objective of this work is to develop and verify a graph theory-based approach for predicting the temperature distribution in metal AM parts. This objective is consequential to overcome the current poor process consistency and part quality in AM. One of the main reasons for poor part quality in metal AM processes is ascribed to the nature of temperature distribution in the part. For instance, steep thermal gradients created in the part during printing leads to defects, such as warping and thermal stress-induced cracking. Existing nonproprietary approaches to predict the temperature distribution in AM parts predominantly use mesh-based finite element analyses that are computationally tortuous—the simulation of a few layers typically requires several hours, if not days. Hence, to alleviate these challenges in metal AM processes, there is a need for efficient computational models to predict the temperature distribution, and thereby guide part design and selection of process parameters instead of expensive empirical testing. Compared with finite element analyses techniques, the proposed mesh-free graph theory-based approach facilitates prediction of the temperature distribution within a few minutes on a desktop computer. To explore these assertions, we conducted the following two studies: (1) comparing the heat diffusion trends predicted using the graph theory approach with finite element analysis, and analytical heat transfer calculations based on Green's functions for an elementary cuboid geometry which is subjected to an impulse heat input in a certain part of its volume and (2) simulating the laser powder bed fusion metal AM of three-part geometries with (a) Goldak's moving heat source finite element method, (b) the proposed graph theory approach, and (c) further comparing the thermal trends predicted from the last two approaches with a commercial solution. From the first study, we report that the thermal trends approximated by the graph theory approach are found to be accurate within 5% of the Green's functions-based analytical solution (in terms of the symmetric mean absolute percentage error). Results from the second study show that the thermal trends predicted for the AM parts using graph theory approach agree with finite element analyses, and the computational time for predicting the temperature distribution was significantly reduced with graph theory. For instance, for one of the AM part geometries studied, the temperature trends were predicted in less than 18 min within 10% error using the graph theory approach compared with over 180 min with finite element analyses. Although this paper is restricted to theoretical development and verification of the graph theory approach, our forthcoming research will focus on experimental validation through in-process thermal measurements.

[DOI: 10.1115/1.4043648]

Keywords: additive manufacturing, thermal modeling, temperature distribution, graph theory

1 Introduction

1.1 Objective. The goal of this work is to understand the effect of process parameters and part design (part geometry) on the instantaneous spatiotemporal distribution of temperature, also called thermal field or temperature history, in metal parts as they are being built (printed) layer-by-layer using additive manufacturing (AM) processes [1]. As a step toward this goal, the objective of this work is to develop and verify a graph theory-based approach for predicting the spatiotemporal distribution of temperature in metal AM parts.

Figure 1(a) shows the laser powder bed fusion (LPBF) AM process in which layers of metal powder are rolled or raked

across a build plate and selectively melted using a laser to form the part. Figure 1(b) shows a schematic of a directed energy deposition (DED) metal AM process, wherein a stream of metal powder material is directed onto a substrate via nozzles. The powder is melted through the thermal action of a laser. By translating the nozzle relative to the substrate in the horizontal and vertical planes, a desired part geometry is built layer-upon-layer [2].

1.2 Motivation for Thermal Modeling in Metal Additive Manufacturing. Metal AM processes, such as LPBF and DED, offer significant advantages over conventional subtractive and formative manufacturing processes, including design flexibility and shorter lead times [3–5]. However, poor process consistency and inferior part quality currently afflict metal AM processes [6–11]. Given the uncertainty in part quality, precision-oriented strategic sectors, such as aerospace and biomedical, are reluctant to deploy metal AM processes for making safety-critical parts. The three

¹Corresponding author.

Manuscript received October 19, 2018; final manuscript received April 23, 2019; published online May 21, 2019. Assoc. Editor: Kevin Chou.

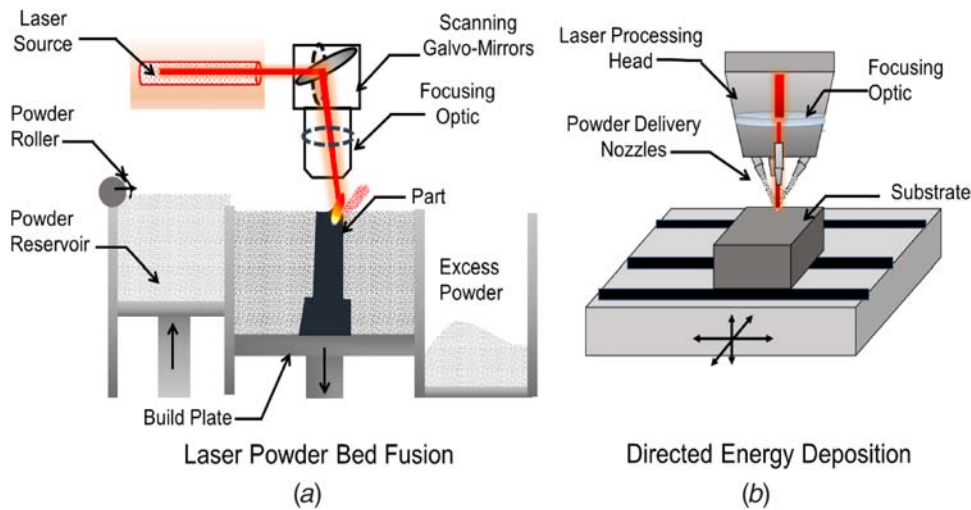


Fig. 1 The schematic of the (a) laser powder bed fusion (LPBF) and, (b) blown powder directed energy deposition (DED) metal AM processes

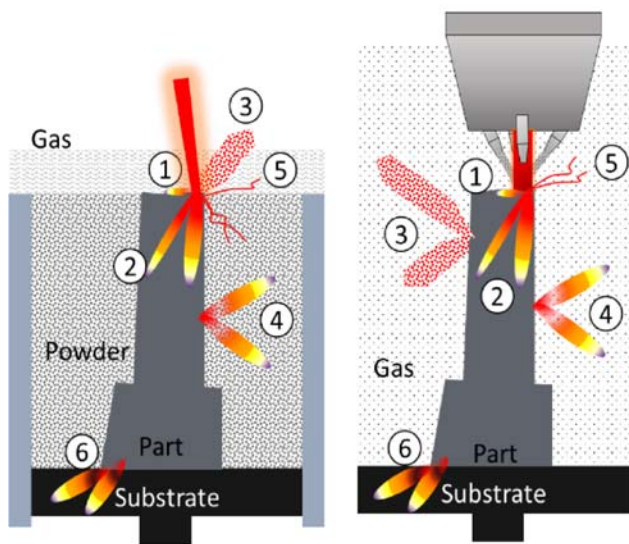
main process-related reasons that impede the quality of metal AM parts are [12]

- (1) Inconsistency in the as-built microstructure, termed as microstructural heterogeneity [13–15].
- (2) Porosity formation, which includes the case of poor consolidation of the material called lack-of-fusion porosity due to insufficient input energy to melt the material as well as vaporization of the powder material due to excessive input energy called pinhole porosity [16,17].
- (3) Deviations in the as-built geometry from its intended design due to distortion. At the part-level, other defects, besides distortion, include cracking and delamination of layers.

The aforementioned flaws are largely governed by thermal phenomena, specifically, the magnitude and direction of heat flow in the part as it is being built—called the temperature field or

thermal history [12,18,19]. To explain further, the salient thermal phenomena in LPBF and DED, stratified by the various energy part–process interaction zones, are represented in Fig. 2 [20,21]. The thermal phenomena depicted in Fig. 2 encompass complex conductive, convective, and radiative heat transfer interactions between the part, energy source, material, and chamber (powder as well as gas) [22]. These thermal aspects in AM, which govern the temperature distribution in the part, are in turn a function of the material, part design, and the process parameters, such as the power and velocity settings of the laser used for melting the material [23].

Statistical experimentation methods to obtain the desired geometry and microstructure in AM will involve building test parts by adjusting process parameters, followed by destructive materials characterization. Such a statistically designed experiments-based approach is prohibitively expensive and may not be viable in metal AM given the small batch sizes, vast parameter space (there



Laser Powder Bed Fusion

Directed Energy Deposition

Salient Thermal Phenomena in Metal AM.

- ① *Part-Energy Source Interaction Zone*
Latent Heat of Melting & Solidification.
Meltpool Marangoni Convection
- ② *Part-Part Interaction Zone*
Conductive Heat Transfer
- ③ *Part-Gas Interaction Zone*
Radiative Heat Transfer
- ④ *Part-Powder Interaction Zone (LPBF)*
Part-Gas Interaction Zone (DED)
Convective Heat Transfer
- ⑤ *Energy Source-Part-Powder Interaction Zone (LPBF)*
Reflection, Absorption, Keyhole melting-effect
Laser-Part-Gas Interaction Zone (DED)
Reflection
- ⑥ *Part-Substrate Interaction Zone*
Conduction

Fig. 2 The salient heat transfer modes in LPBF and DED encompassing complex interactions among the part, material, energy source, and environment (surrounding inert gas)

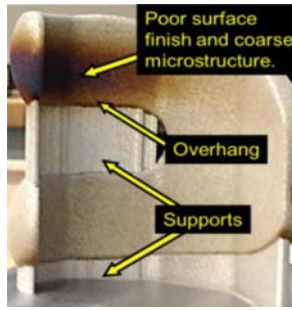


Fig. 3 LPBF knee implant with an overhang feature shows poor surface finish and coarse microstructure

are over 50 variables in LPBF alone), and the slow nature of AM processes compared with conventional manufacturing [24,25].

Furthermore, owing to the tight coupling of the part design, material properties, and parameters to the temperature distribution, a set of parameters optimized for a particular part geometry and material are not readily transferable to a new part design and material [8]. Therefore, as emphasized by several researchers, to ensure part quality in metal AM, it is imperative to understand and explain the following intertwined links in the LPBF process chain through quantitative modeling [26–31]: part design, process parameters, and material characteristics → temperature distribution (thermal history) → microstructure and geometry flaws [32–35].

The burgeoning need for a formal framework based on a fundamental understanding of the thermal physics of the process to guide the design of the AM parts and parameter selection is practically illustrated in Fig. 3, which shows a biomedical knee implant built by the authors using the LPBF process [36]. This part has a feature called an overhang whose underside is not supported. To prevent the part from collapsing under its own weight, supports were automatically built under the overhang feature by the native software on the LPBF machine. Nonetheless, after the build, the overhang area was found to have coarse-grained microstructure, distortion, and poor surface finish, which makes the implant potentially unsafe for clinical use.

Such defects, also reported in the literature by other researchers, result from the heat being constrained in the overhang section [36–40]. The reason for the constrained heat in the overhang section is hypothesized due to the low thermal conductivity of the surrounding metal powder and the thin cross-sectional area of the supports. Through accurate and computationally efficient thermal simulations that can predict the effect of process conditions and part design on the spatiotemporal distribution of temperature, the occurrence of defects, such as geometric deformation and microstructure heterogeneity, can be minimized without extensive empirical optimization [41].

Accurate quantitative modeling approaches based on finite element (FE) analyses have been successfully developed and applied for understanding the thermal aspects of AM at the part-level as summarized in Refs. [11,12,42–44] and will be discussed in depth in Sec. 2. However, these pioneering nonproprietary approaches reported in the published literature are computationally expensive, with simulation of a few deposited layers amounting to many hours, if not days [45,46]. For example, Cheng et al. reported that the computation time for thermomechanical analysis for a 6 mm cuboid shape part exceeds 92 h [45].

Hence, newer efficient approaches are needed to predict the temperature distribution, given different part designs and process parameters. In the context of FE-based modeling, we note that certain commercial, proprietary approaches, such as Autodesk's NETFABB and Ansys 3DSim, have leveraged adaptive meshing principles to drastically reduce the computational time. However, the underlying mathematics of these commercial software applications is proprietary [43,47].

1.3 Novelty and Advantages of the Proposed Graph Theory Approach. Within the context of prediction of the temperature field, the advantages of using the graph-theoretic approach are twofold:

- (1) Reduced computational burden due to elimination of mesh-based analysis

Predicting the temperature field in metal AM involves solving the continuum heat equation (Eqs. (1) and (2) in Sec. 3.2). Instead of solving the heat diffusion equation for each element through element birth-and-death techniques as in FE analysis, we track the temperature in the part in terms of discrete nodes of a planar graph projected onto its geometry. In other words, we solve the discrete counterpart of the continuum heat diffusion equation (Eq. (3)). Our efforts in verifying results from the graph-theoretic approach with the FE analysis, described in Sec. 4.2, leads us to infer that a significant portion of the computation effort in FE analysis is consumed by the meshing of elements and simulation of the birth-and-death process to mimic material deposition in AM. The graph-theoretic approach circumvents the need for meshing, and as a result, the computation time for simulation of AM processes can be considerably reduced compared with the existing, nonproprietary FE analysis-based approaches.

- (2) Elimination of matrix inversion steps required to solve the heat diffusion equation.

While FE analysis rests on matrix inversion steps to solve the heat diffusion equation for each of the thousands of elements, the graph-theoretic method instead relies on the more computationally tractable matrix multiplication operations to obtain the eigenvectors (Φ) and eigenvalues (Λ) of the graph Laplacian (L) (to be discussed subsequently in Sec. 3.3), which greatly reduces the computational burden.

By reducing the computational time in predicting the temperature distribution to minutes, as opposed to hours, estimating the geometric distortion and microstructural evolution that are governed by the thermal history becomes considerably more tractable. Furthermore, the near real-time predictions of the temperature distribution made possible through the proposed approach lays the foundation for feed-forward, model-based control of metal AM as opposed to data-driven machine learning and analytics.

1.4 Organization of the Paper. The rest of this paper is organized as follows. The literature concerning the FE-based thermal modeling of metal AM processes at the part-level is outlined in Sec. 2. Next, the graph-theoretic approach is described in Sec. 3, wherein we show that the eigenvectors (Φ) and eigenvalues (Λ) of the Laplacian matrix (L) solve the heat diffusion equation, which governs temperature distribution in AM parts. We dedicate Sec. 4 of this paper to the verification of the graph theory approach through the following two studies: (1) verifying the thermal trends obtained from graph theory with exact Green's function-based analytical method and finite element analysis for an elementary cuboid geometry and (2) comparing the thermal trends derived using graph theory approach for three-part geometries in an LPBF simulation scenario with the thermal trends obtained by implementing Goldak's moving heat source FE analysis solution, and Autodesk's NETFABB software. This paper closes in Sec. 5 with conclusions and avenues for future work.

2 Prior Research in Finite Element Modeling in Metal Additive Manufacturing Processes

It is beyond the scope of this paper to provide an in-depth exposition of the vast and mature area of FE analysis in AM, which is the de facto means to solve the heat diffusion equation described later in Sec. 3 as applied to metal AM. The reader is referred to the recent

book by Denlinger et al. [43], which comprehensively details the methodological implications, challenges, and practical application concerning FE-based thermomechanical analysis in AM.

Comprehensive review articles on part-level thermal modeling in AM with the finite element method in metal AM have been recently published by Luo and Zhao [48], Bandyopadhyay and Traxel [42], and DebRoy et al. [11]. These articles provide an in-depth review of the strategies that have been advanced by researchers to reduce the computational burden of FE analysis in AM; a summary of these is provided below.

(1) Adaptive meshing and element activation schema

Researchers have simplified the meshing process, such as consolidating layers into blocks or super layers using an adaptive mesh refinement and coarsening strategy [46]. The key idea is that certain areas of the part where the cross section and boundaries change sharply have finer mesh while the rest of the part may have a coarser mesh. Further, researchers in metal AM have adapted two main approaches to simulate the deposition of the material in the FE framework [49]. In the first approach, called the inactive element method, elements are incrementally added when the melting process is initiated. Though the inactive approach closely mimics the AM processes, it is challenging to implement because the number of elements increases as the part grows. The second technique is called the quiet element method, wherein the part is meshed *a priori*, but only elements in the current layers and those below are thermally active. The properties of the elements in the succeeding layers are deliberately altered to have no thermal effect. To reduce the computational burden, commercial approaches, such as NETFABB (Autodesk), have taken two tasks:

- (i) adaptive mesh refinement of the part, such that certain areas have large or coarser nodes and
- (ii) using a hybrid meshing approach combining quiet and inactive meshing schema. Such a hybrid element activation schema was pioneered by Michaleris and is reported to be implemented in NETFABB [49].

(2) Simplification of the process physics

As first described in Fig. 2, the main heat transfer mechanisms in the process are

- (i) conductive heat losses at the part and substrate level, wherein the heat on the top surface travels through the solidified layers in the bottom, and further through the substrate;
- (ii) radiative heat loss at the top surface to the process chamber;
- (iii) loss due to convection at the boundary of the printed part and the surrounding powders and inert gas, such as argon, that is filled in the chamber; and
- (iv) latent heat involved at the melt-pool zone as the material state changes from solid to liquid, and back to solid again on cooling.

Incorporating all these heat transfer mechanisms in a model will inordinately increase its computational burden. Consequently, researchers resort to simplifications, such as ignoring latent heat effects from the melt-pool; maintaining static material properties, such as a constant heat conduction rate, density and specific heat; and, ignoring the radiative heat losses into the chamber and the convective heat losses into the surrounding powder by assuming the part to be completely insulated. Some of these simplifications have been shown to have a significant effect on the prediction of the thermal trends [41].

(3) Simplifying the part geometry, energy source, and powder bed-related conditions.

Researchers seek to reduce the computational burden by simplifying the part geometry, such as simulating only one half of a symmetric part or considering deposition in the form of super layers

[44]. Furthermore, the behavior of the energy source is also simplified by assuming heating of an entire layer at once, or in terms of rectilinear hatches, as opposed to complicated island type scanning. The thermal models can also incorporate strategies to simplify the effect of the energy source by approximating the shape of the beam, e.g., assuming Gaussian, ellipsoidal, and tophat shapes. Mesh-free approaches for thermal modeling in AM are being explored, such as electric network type modeling schema introduced by Peng et al. [50] and discrete finite difference modeling by Ganeriwala and Zohdi [51,52].

From a graph-theoretic perspective, a review paper by Solomon [53] discusses discrete differential operators that arise from partial differential equations such as the heat equation; it shows that the Laplacian matrix constructed from a uniformly spaced grid gives a solution to the heat diffusion equation. However, if the grid is not equally spaced, the relationship to the correct solution of the heat equation is not clear. In a study of geometric surface smoothing, Belkin et al. [54] assert that their discrete Laplacian matrix approaches the continuous Laplacian in the limit as the grid becomes sufficiently fine, even if the grid pattern is nonuniform. Their algorithm includes multiplicative factor $1/\epsilon^2$ where ϵ which is the size of the neighborhood of influence for nearby grid points. In a study of image smoothing, Zhang and Hancock use randomly assigned node locations to construct a discrete Laplacian matrix and subsequently to solve the heat diffusion equation [55].

In closing this section, we note that the proposed graph-theoretic approach is distinct from the mesh-free methods developed for peridynamics of systems undergoing dynamic cracking [56,57], and it is also different from spectral collocation methods where splines provide an *a priori* functional form of the solution as part of a standard matrix inversion process [58,59].

3 The Graph-Theoretic Approach for Approximating the Temperature Distribution in Additive Manufacturing Parts

3.1 Assumptions of the Graph-Theoretic Model. To keep the development brief, the following simplifying assumptions are applied to the graph-theoretic approach.

- *Heat transfer-related assumptions.* The thermal properties of the material are static, in that, they do not change as the material changes state from particulate matter to a liquid (melt-pool formation), and then back to a solid. In other words, the latent heat of melting and solidification is ignored. The heat loss due to vaporization, and material composition and density changes due to mass transfer are also not considered. Likewise, the radiative effects from the top surface of the part are not accounted for.
- *Energy source-related assumptions.* The laser is considered a moving point heat source, i.e., the beam diameter and shape, and subsequent diffusion of the laser on the powder bed surface are not accounted for. It is assumed that the laser rays are completely absorbed in the topmost layer and are not repeatedly reflected by the powder. Hence, effects such as keyhole melting and variations in thermal absorptivity contingent on powder packing density on the powder bed are ignored [21].
- *Powder bed-related assumptions.* There is only one single part in the build plate at a given time, hence there is no heat exchanged with other parts. The powder bed is considered to be at the same temperature as the chamber and that the packing density of the powder bed remains static. Lastly, in the context of LPBF, low-temperature nodes (ambient temperature nodes) belonging to the next layer are deposited on the previous printed layer to simulate deposition, and the newly deposited nodes in each hatch (or layer, if a coarse simulation is desired) are heated by the laser beam, to simulate the fusion

process. No heat transfer occurs until a hatch (or layer) is completely fused.

These assumptions can be relaxed to provide a more comprehensive model, which will be pursued in later works by the authors.

3.2 The Heat Diffusion Equation and its Connection to Temperature Distribution in Additive Manufacturing Parts.

As stated previously, the objective of this work is to develop and apply a graph-theoretic approach to predict the temperature history in metal AM parts. To realize this objective, we solve the heat diffusion equation

$$\rho c_p \frac{\partial T}{\partial t} - k \left(\frac{\partial^2}{\partial x^2} + \frac{\partial^2}{\partial y^2} + \frac{\partial^2}{\partial z^2} \right) T = E_v \quad (1)$$

In Eq. (1), T is the instantaneous temperature at a location $\{x, y, z\}$ at time t . The AM process parameters are captured in the energy density, E_v , which is the energy supplied by the laser to the top layer to melt a unit volume of material per second; $E_v = P/h_l \cdot d \cdot l$ (W/mm^3), where P is the laser power in (W), h_l is the width of the laser track or hatch (mm), d is the layer height (mm), and l is the length melted in 1 s (mm). The material properties are encapsulated in the following terms: density ρ (kg/m^3), specific heat c_p ($\text{J}/(\text{kg K})$), and thermal conductivity k ($\text{W}/(\text{m K})$).

From the AM perspective, the term $\partial T/\partial t$ is analogous to the rate of change of temperature at a particular point in the part referenced by its spatial coordinates $\{x, y, z\}$ as it is heated by a moving energy source, e.g., a laser in LPBF, while being consolidated layer-upon-layer. Solving the heat equation results in the instantaneous temperature $T(x, y, z, t)$ at a time t for a Cartesian spatial coordinate $\{x, y, z\}$. The temporal map of $T(x, y, z, t)$, i.e., the trace of the temperature T at the location $\{x, y, z\}$ over time, gives the thermal history in the part for that location.

The graph theory approach to the solution of the heat diffusion equation relies upon two approximations. First, the source term, E_v , in Eq. (1) is replaced by an initial temperature distribution, for which the portion of the AM part that is scanned by the laser is assigned an elevated temperature to represent, for example, the metal fusion temperature. The heat equation is solved repeatedly, again and again, following each laser scan. Specifically, consider a spatial point $\{x, y, z\}$ during the AM process, immediately after a laser scan is completed, the heat diffusion equation to be solved takes the form

$$\frac{\partial T}{\partial t} - \alpha \left(\frac{\partial^2}{\partial x^2} + \frac{\partial^2}{\partial y^2} + \frac{\partial^2}{\partial z^2} \right) T = 0 \quad (2)$$

$$T(x, y, z, t = 0) = T_o(x, y, z)$$

In Eq. (2), T_o is the initial condition and $\alpha = k/(\rho c_p)$ is the thermal diffusivity. Further, the second-order spatial derivative ($\partial^2/\partial x^2 + \partial^2/\partial y^2 + \partial^2/\partial z^2$) is called the continuous Laplacian operator and typically represented by the symbol Δ .

The solution of the above heat diffusion equation describes the evolving temperature in the AM part in the time period between one laser scan and the next. After a layer is completely processed, the build platen is lowered, and a new layer of powder is deposited over the top of the previous layer. When the new layer is deposited and scanned by the laser, an update to the computational domain is required along with a new initial condition. These updates necessitate a recomputation of the heat equation. This rationale is valid even when a more granular laser hatch-by-hatch evolution of the process is simulated. To explain further, the new computational domain includes the newly fused layer of metal powder at an elevated temperature on top of the previously fused metal whose initial temperature is the end point of the previous temperature computation. Just as the part is created layer-by-layer (or

hatch-by-hatch), the temperature solution is computed in many small discrete increments of time.

A mathematical premise key to the graph theory approach is that the spatial derivatives represented by the continuous Laplacian operator (Δ) in the above continuum heat diffusion equations, Eq. (2), can be replaced by a discrete counterpart (\mathbf{L}), and the continuously varying temperature T can be replaced by a vector of discrete temperatures \mathbf{T} at M sampled nodal points in the domain of the part. The discrete form of the heat diffusion equation, with vectors in bold typeface may be written as

$$\frac{\partial \mathbf{T}}{\partial t} + \alpha \mathbf{L} \mathbf{T} = 0 \quad (3)$$

subject to the initial condition

$$\mathbf{T}(x, y, z, t = 0) = \mathbf{T}_o(x, y, z)$$

Note the sign change in Eq. (3), as the Laplacian matrix \mathbf{L} from graph theory is defined with a sign opposite to that of the continuous spatial derivatives (Δ) present in the continuum heat equation (Eq. (2)). If the discrete form of the heat diffusion equation (Eq. (3)) is applied to a uniformly spaced grid of nodal points, a discrete Laplacian matrix (\mathbf{L}) can be constructed to reproduce the well-known finite difference approximation [60].

The mathematical proof of the graph theory-based solution to the heat equation Eq. (2) is discussed in the forthcoming Sec. 3.3.

3.3 Solution to the Heat Equation Using Graph Theory.

In the discrete heat diffusion equation in Eq. (3), \mathbf{T} is a column vector for the temperature at each of M nodes in the domain and \mathbf{L} is the $[M \times M]$ Laplacian matrix. For boundary conditions of type Dirichlet, Neumann, and Robin (types 1, 2, and 3, boundary conditions, respectively), it is shown by Saito that the eigenvalues (Λ); of the discrete Laplacian operator are discrete and nonnegative, and the eigenvectors are orthogonal, i.e., $\langle \phi_i, \phi_j \rangle = 0$, assuming that the domain of the Laplacian is bounded, connected, and compact [61]. The particular form of the Laplacian matrix discussed here and described in Eqs. (6)–(12), is diagonally dominant and symmetric, i.e., positive semidefinite.

Accordingly, the orthogonality of eigenvectors (Φ) and nonnegativity of eigenvalues (Λ) of the Laplacian matrix (\mathbf{L}) is preserved [62]. The eigenvectors and eigenvalues of the Laplacian matrix are found with standard matrix methods and satisfy the following eigenvalue equation, $\mathbf{L}\Phi = \Phi\Lambda$. Here, Φ is the right eigenvector matrix in which each column contains one of M eigenvectors, and Λ is a diagonal matrix containing nonnegative eigenvalues ranked in order from the smallest in row 1 to the largest in row M . Because the transpose of an orthogonal matrix is the same as its inverse, that is, $\Phi^{-1} = \Phi'$, and $\Phi\Phi' = \mathbf{I}$, then the above eigenvalue equation may be post multiplied by Φ' to obtain $\mathbf{L} = \Phi\Lambda\Phi'$.

Replacing this relationship into the discrete heat diffusion equation Eq. (3) we obtain

$$\frac{\partial \mathbf{T}}{\partial t} + \alpha (\Phi\Lambda\Phi') \mathbf{T} = 0$$

This first-order ordinary differential equation has the solution

$$\mathbf{T} = e^{-\alpha g (\Phi\Lambda\Phi') t} \mathbf{T}_o \quad (4)$$

where g (m^{-2}) is a gain factor that we have added to calibrate the solution and adjust the units. Hence, the heat equation solution contains the eigenvectors and eigenvalues of the graph Laplacian \mathbf{L} . This formal matrix solution gives the temperature vector \mathbf{T} , which contains a value for every spatial node, subject to the initial condition vector \mathbf{T}_o . This solution can be simplified further for improved computational efficiency by considering the Taylor series expansion of the term $e^{-\alpha g (\Phi\Lambda\Phi') t}$, and substituting $\Phi\Phi' = \mathbf{I}$, as shown by

Zhang and Hancock [55] and Bai and Hancock [63] as follows:

$$e^{-\alpha g(\Phi\Lambda\Phi')t} = I + \frac{(-\alpha g(\Phi\Lambda\Phi')t)}{1!} + \frac{(-\alpha g(\Phi\Lambda\Phi')t)^2}{2!} + \frac{(-\alpha g(\Phi\Lambda\Phi')t)^3}{3!} + \dots$$

$$e^{-\alpha g(\Phi\Lambda\Phi')t} = I - \alpha g t \frac{\Phi\Lambda\Phi'}{1!} + \alpha^2 g^2 t^2 \frac{(\Phi\Lambda\Phi')(\Phi\Lambda\Phi')}{2!} - \alpha^3 g^3 t^3 \frac{(\Phi\Lambda\Phi')(\Phi\Lambda\Phi')(\Phi\Lambda\Phi')}{3!} + \dots$$

$$e^{-\alpha g(\Phi\Lambda\Phi')t} = I - \frac{\Phi\Lambda g t \Phi'}{1!} + \frac{\Phi(\Lambda g t)^2 \Phi'}{2!} - \frac{\Phi(\Lambda g t)^3 \Phi'}{3!} + \dots$$

Thus, replacing $e^{-\alpha g(\Phi\Lambda\Phi')t} = \Phi e^{-\alpha g \Lambda t} \Phi'$ in Eq. (4) gives Eq. (5)

$$\mathbf{T} = \Phi e^{-\alpha g \Lambda t} \Phi' \mathbf{T}_0 \quad (5)$$

This expression is the key to the computational efficiency of our approach because the temperature at successive time steps is computed by matrix multiplication only. In contrast, finite element or finite difference methods require a matrix inversion at every time step, at a great computational cost.

As an aside, there is a connection between the Laplacian for graph theory in Eq. (3) and the discrete spatial derivatives involved in the finite difference method. Specifically, under the right conditions (uniform grid spacing and certain edge weights), a Laplacian matrix can be constructed that reproduces the discrete spatial derivatives of the finite difference method [60]. This connection is valuable because the finite difference method has been shown, in the limit as the internodal spacing approaches zero, to be exact [60]. The point to be made here is that the level of approximation for the spatial derivatives in the graph-theoretic approach is related to that of the well-known finite difference method. However, it is also important to note that the graph-theoretic solution of Eq. (3), as outlined above, is distinct from that of the traditional finite difference method. It is the combination of the graph-theoretic Laplacian

matrix (\mathbf{L}) and the efficient solution method of Eq. (3) that makes the graph-based approach unique.

3.4 Steps in Predicting the Temperature Distribution in Additive Manufacturing Parts Using Graph Theory. The approach has the following four steps, as pictorially shown in Fig. 4, and in Fig. 5 as a flowchart diagram. The steps are as follows, with respect to the LPBF process:

- (1) Obtain the geometry of a part and convert it to a set of discrete nodes. Slice the part into layers and hatches. Record the position of each node, in terms of its Cartesian $\{x, y, z\}$ coordinates, and the layer and hatch in which the node is located.
- (2) Construct a network graph from the discrete nodes sampled in step (1). In this step, each of the nodes is connected to other nodes within an ε neighborhood distance (or envelope). In other words, nodes within a spherical radius of ε are connected to each other.
- (3) (a) Simulate the heating of a layer, hatch-by-hatch, and diffuse the heat through the network graph constructed on the nodes sampled in the part, noting that only the nodes in the current layer and below are active and (b) after the heat diffuses through the part, simulate the deposition of a new layer on top of the old layer.
- (4) At each iteration of step 3, the temperature at each node at each time step is recorded in terms of the temperature vector \mathbf{T} . Step 3 is repeated until the part is built.

We note that in Fig. 4 the powder surrounding the part is not shown. The particular C-shaped geometry and the reason for heat accumulation in the overhang region of this part as depicted in Fig. 4, step 4 is studied and explained in depth in Sec. 4.2.

Step 1: Obtain the geometry of a part and converting it to a set of discrete nodes

Process parameters and the part geometry are declared in this step. The part is sliced into layers, representative of the layer thickness, and a fixed number (M) of spatial locations are randomly sampled in each layer. In the later step 4, the temperature distribution in the part is observed and stored (recorded) at these M fixed spatial locations, termed nodes.

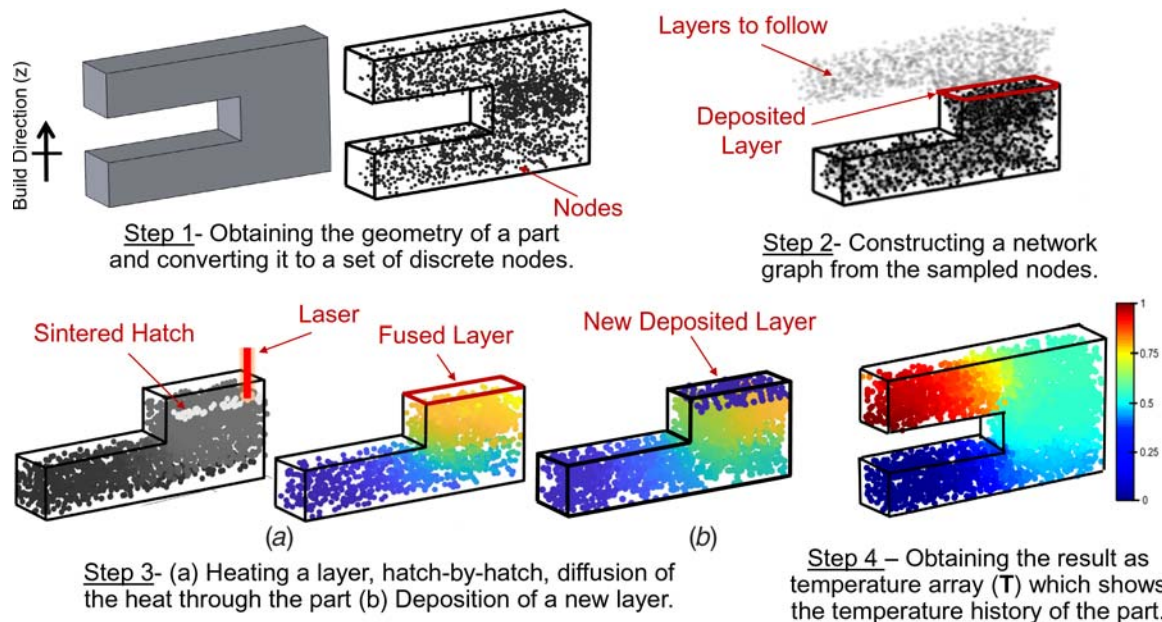


Fig. 4 The four steps in the spectral graph-theoretic approach used to estimate the temperature distribution in the part layer-by-layer. Here, we show an embodiment of the LPBF process. The powder particles surrounding the part are not shown in this figure.

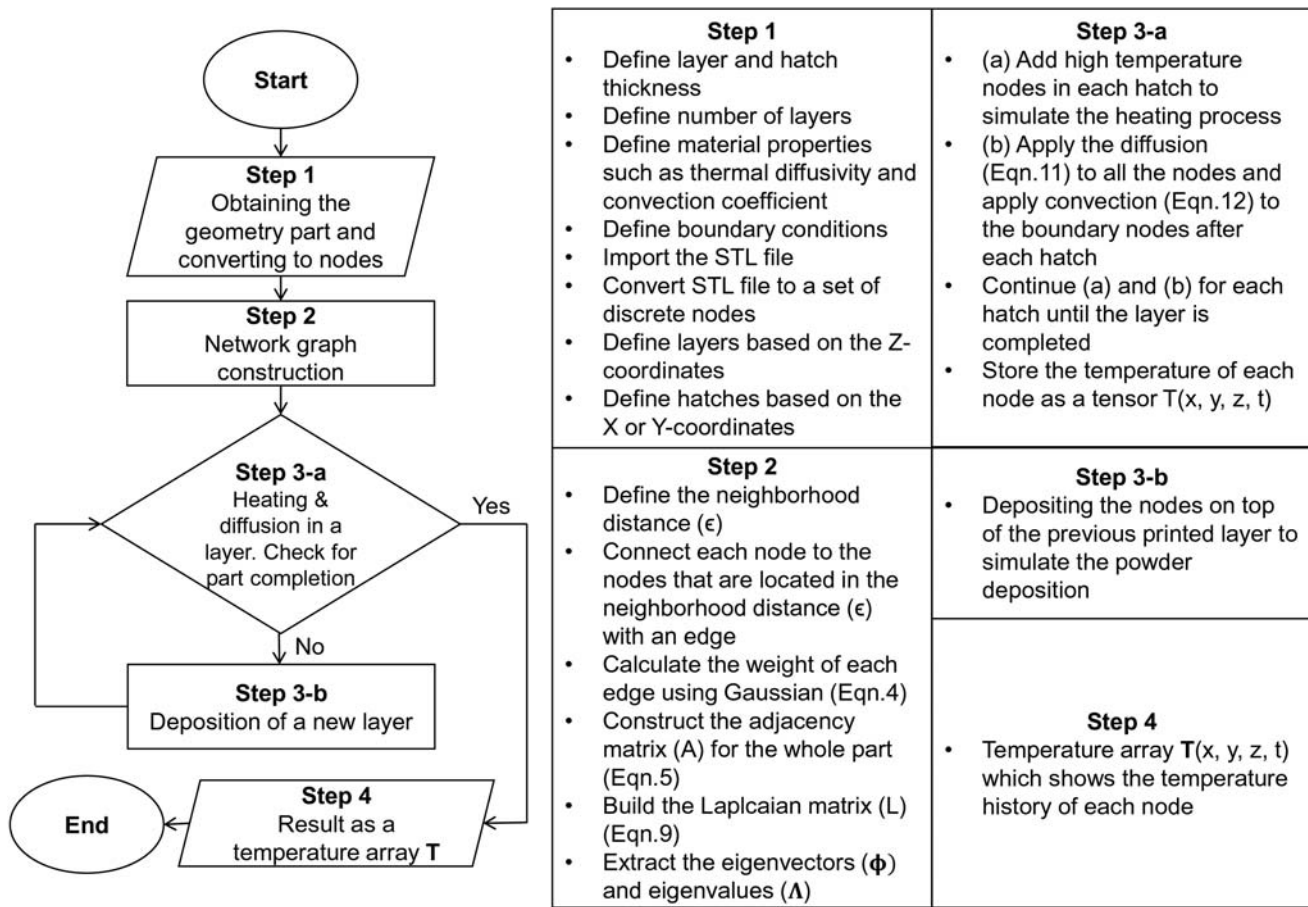


Fig. 5 The flowchart of four steps in the graph-theoretic approach in context of LPBF process

The random sampling of the nodes is done to reduce the computational burden of the approach. The number of nodes sampled is contingent on the geometry of the part, in this work (Sec. 4.2), a density of 5 nodes per mm^3 provided a sufficiently good approximation (relative error $\approx 10\%$) of the thermal trends estimated with a moving heat source solution obtained through FE analysis [64,65].

Step 2: Network graph construction

In graph theory, a concept of discrete mathematics, a graph consists of nodes and the edges that connect them [62]. Here, nodes are spatial points sampled in the part and the edges are the links among the nodes. We begin by constructing a graph over the set of M nodes sampled in Step 1. The aim is to connect a pair of nodes π_i and π_j within an ϵ neighborhood distance. Consider $c_i = \{x_i, y_i, z_i\}$ as the location of the node π_i , and $c_j = \{x_j, y_j, z_j\}$ as the location of the node π_j , then the weight of the edge connecting node π_i and π_j is expressed in mathematical terms below, with a Gaussian radial basis function

$$a_{ij} = \begin{cases} e^{-(c_i - c_j)^2 / \sigma^2}, & (c_i - c_j)^2 \leq \epsilon \\ 0, & (c_i - c_j)^2 > \epsilon \end{cases} \quad (6)$$

where $(c_i - c_j)^2$ is the square of the distance between nodes π_i and π_j . In this work, the term ϵ is akin to the radius of a sphere within which one node is connected to its neighbors, and σ is the standard deviation of the pairwise distances $(c_i - c_j)^2$.

We note that Eq. (6) embodies the Gaussian law in that, if two nodes are closer, their weight will be proportionally larger. We further note that a_{ij} takes a value between 0 and 1.

Next, we place each element a_{ij} on the i th row and j th column of the adjacency matrix A . Essentially, the element i th row and j th column of A relates to strength of the edges connecting the nodes π_i and π_j .

$$A = [a_{ij}] \quad (7)$$

$$\lim_{c_i - c_j \rightarrow 0} a_{ij} = 1$$

The matrix A is a symmetric $M \times M$ matrix because $a_{ij} = a_{ji}$. The next step involves computing the degree d_i of a node π_i , i.e., the aggregate of the strength of the edges that are connected to the node π_i . The degree of node π_i is computed by summing the i th row of the adjacency matrix A .

$$d_i = \sum_j a_{ij} \quad (8)$$

From the degree of node d_i , the Laplacian l_{ij} at node i is defined as follows:

$$l_{ij} \stackrel{\text{def}}{=} d_i - a_{ij} \quad (9)$$

We note that $\sum_j l_{ij} = 0$. The diagonal degree matrix D is formed from d_i 's as follows:

$$D = \begin{bmatrix} d_1 & \cdots & 0 \\ \vdots & \ddots & \vdots \\ 0 & \cdots & d_M \end{bmatrix} \quad (10)$$

then given the adjacency matrix \mathbf{A} , the discrete Laplacian \mathbf{L} can be cast in matrix form as

$$\mathbf{L} \stackrel{\text{def}}{=} (\mathbf{D} - \mathbf{A}) \quad (11)$$

Finally, the Eigen spectra of the Laplacian \mathbf{L} is computed as follows:

$$\mathbf{L}\boldsymbol{\phi} = \boldsymbol{\phi}\boldsymbol{\Lambda} \quad (12)$$

where $\boldsymbol{\phi}$ are the eigenvectors and $\boldsymbol{\Lambda}$ are the eigenvalues of \mathbf{L} . We note that \mathbf{L} is a real, diagonally dominant symmetric matrix, with positive diagonal entries, and negative off-diagonal entries. Due to these properties, \mathbf{L} falls under the category of a Stieltjes matrix and has nonnegative eigenvalues ($\boldsymbol{\Lambda}$) and orthogonal eigenvectors ($\boldsymbol{\phi}$) [62]. In other words, $\langle \boldsymbol{\phi}_i, \boldsymbol{\phi}_j \rangle = 0, \forall i \neq j; i, j = \{1, 2, \dots, M\}$, and each of the M individual eigenvalues are nonnegative $0 = \lambda_1 < \lambda_2 < \dots < \lambda_M$.

Step 3: (a) Heating a layer, hatch-by-hatch, diffusion of the heat through the part and (b) deposition of a new layer

In step 3(a), the heat from the laser is applied to the topmost layer in the form of hatches. The magnitude of heat applied is E_V (W/m^3), where the time taken to fuse a hatch is considered infinitesimal compared with the time taken to build the whole layer or the time it takes the bed to be lowered and to the recoater to deposit a new layer. The heat diffuses to the rest of the part within the powder bed, and through the substrate in the time (t). The eigenvectors $\boldsymbol{\phi}$ of the Laplacian \mathbf{L} provide a discrete solution to the heat equation, specifically, if $\boldsymbol{\phi}'$ is the transpose of $\boldsymbol{\phi}$, then the temperature profile observed at a discrete time step t for a node at position (x, y, z) below the top layer is given by the following, the mathematical justification for which was given in the preceding Sec. 3.3.

$$T = \boldsymbol{\phi} e^{-\alpha g \Delta t} \boldsymbol{\phi}' T_0 \quad (13)$$

where T_0 is the initial temperature distribution introduced to simulate laser heating. The material-related factors are contained in the term α (m^2/s) and g is a constant *gain factor* (m^{-2}). Lastly, we need to account for the heat loss due to convection at the boundary of the powder and part. For this purpose, we demarcate the boundary nodes of the part and adjust the temperature of the boundary nodes (T_b) using Newton's law of cooling

$$T_b = e^{-\tilde{h}(\Delta t)} (T_{bi} - T_p) + T_p \quad (14)$$

where T_p is the temperature of the powder (considered to be equal to the ambient temperature in the environment T_∞), T_{bi} is the initial temperature of the boundary nodes, T_b is the temperature of the boundary nodes after convective heat loss and \tilde{h} is the normalized coefficient of convection from part to the surrounding powder (also called the Biot number), and Δt is the dimensionless time step between laser scans.

In step 3(b), which is only applicable to the LPBF process and not DED, a layer of powder is raked on top of the fused layer. The process repeats through steps 3(a) and (b) until the part is built. At every iteration of step 3, we estimate and store the resulting temperature of each node $T(x, y, z, t)$, inside a temperature vector \mathbf{T} , which eventually in step 4 represents the temperature history and temperature distribution of the whole part.

4 Verification of the Approach

This section is divided into two parts. The first part, described in Sec. 4.1, compares the graph theory approach with the exact Green's function-based analytical solution and finite element solution for heat diffusion in a simple cuboid geometry [66]. The second part, detailed in Sec. 4.2, applies the graph theory approach

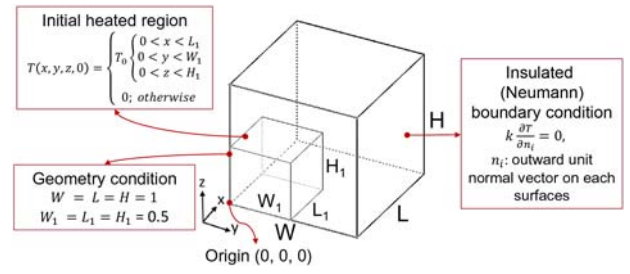


Fig. 6 The cube with an initial heated region and insulated boundaries (Neumann boundary condition)

for predicting the temperature distribution to three-part designs in an LPBF scenario, the results obtained therefrom are compared with Goldak's FE-based solution, and a commercial implementation (NETFABB) [64,65].

4.1 Verification of the Graph Theory Approach for a Cuboid Geometry. This section aims to quantify the accuracy of the graph theory-derived thermal history by comparison with analytical and finite element solutions for a simple test case. This test case simulates heat diffusion in a cube. The cube is assumed to be insulated on the boundaries (Neumann boundary condition), which results in internal heat dispersion until a steady state condition is achieved.

There is a fixed volume inside the cube which is considered to be momentarily heated for a vanishingly small time. Each edge of this heated volume is half that of the larger cube, meaning the volume of the heated section is one-eighth of the entire cube. Figure 6 shows the geometry, initial heated region, and the boundary conditions imposed upon the system. Additional details are available in the author's publications and website [66,67]. The dimension of the cube is taken to be 1 unit.

The case of heat diffusion in a cube can be made dimensionless by the following parameterization:

$$\begin{aligned} \tilde{x} &= \frac{x}{L}; & \tilde{y} &= \frac{y}{W}; & \tilde{z} &= \frac{z}{H}; & \tilde{W} &= \frac{W}{L}; & \tilde{H} &= \frac{H}{L} \\ \tilde{L}_1 &= \frac{L_1}{L}; & \tilde{W}_1 &= \frac{W_1}{W}; & \tilde{H}_1 &= \frac{H_1}{H}; & \tilde{t} &= \frac{\alpha t}{L^2}; & \tilde{T} &= \frac{T - T_0}{T_0} \end{aligned} \quad (15)$$

where L , W , and H are the geometrical dimensions of the cube, L_1 , W_1 , and H_1 are the geometrical dimensions of the heated cube, t is the time, α is the thermal diffusivity, T_0 is the initial temperature, and T is the final temperature. Subsequently, the dimensionless form of the heat equation and boundary value problem for the cube shape are given by

$$\frac{\partial^2 \tilde{T}}{\partial \tilde{x}^2} + \frac{1}{\tilde{W}^2} \frac{\partial^2 \tilde{T}}{\partial \tilde{y}^2} + \frac{1}{\tilde{H}^2} \frac{\partial^2 \tilde{T}}{\partial \tilde{z}^2} = \frac{\partial \tilde{T}}{\partial \tilde{t}}; \quad \begin{cases} 0 < \tilde{x} < 1 \\ 0 < \tilde{y} < 1 \\ 0 < \tilde{z} < 1 \end{cases} \quad (16)$$

At boundary i , we impose the Neumann boundary condition

$$\frac{\partial \tilde{T}}{\partial \tilde{n}_i} = 0, \quad i = 1, 2, 3, 4, 5, 6 \quad (17)$$

$$T(\tilde{x}, \tilde{y}, \tilde{z}, 0) = \begin{cases} T_0 & \begin{cases} 0 < \tilde{x} < \tilde{L}_1 \\ 0 < \tilde{y} < \tilde{W}_1 \\ 0 < \tilde{z} < \tilde{H}_1 \end{cases} \\ 0 & \text{otherwise} \end{cases} \quad (18)$$

where \tilde{n}_i is the outward normal vector from each surface of the cube. The dimensionless form of the analytical diffusion is found by the Green's function (Eq. (19)); see Ref. [67] for a full development of

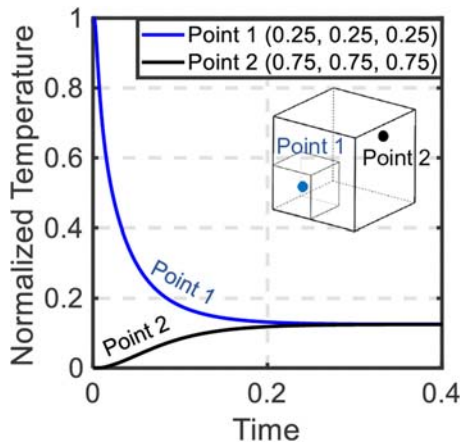


Fig. 7 Analytical diffusion at observation point 1: {0.25, 0.25, 0.25} and observation point 2: {0.75, 0.75, 0.75} from the origin

the solution).

$$T(\tilde{x}, \tilde{y}, \tilde{z}, \tilde{t}) = \left[\tilde{L}_1 + 2 \sum_{m=1}^{\infty} \exp(-m^2 \pi^2 \tilde{t}) \frac{\cos(m\pi \tilde{x}) \sin(m\pi \tilde{L}_1)}{m\pi} \right] \times \left[\tilde{W}_1 + 2 \sum_{n=1}^{\infty} \exp\left(\frac{-n^2 \pi^2 \tilde{t}}{\tilde{W}^2}\right) \frac{\cos(n\pi \tilde{y}) \sin(n\pi \tilde{W}_1)}{n\pi} \right] \times \left[\tilde{H}_1 + 2 \sum_{p=1}^{\infty} \exp\left(\frac{-p^2 \pi^2 \tilde{t}}{\tilde{H}^2}\right) \frac{\cos(p\pi \tilde{z}) \sin(p\pi \tilde{H}_1)}{p\pi} \right] \quad (19)$$

Here, $m\pi$, $n\pi$, and $p\pi$ are eigenvalues along the x , y , and z directions, respectively. The steady state is considered the moment that observation points reach to an equal temperature up to the fourth decimal point. The temperature is observed at two observation points inside the cube as follows: point 1 (0.25H, 0.25L, 0.25W) and point 2 (0.75H, 0.75L, 0.75W). The thermal trends at points 1 and 2 from

the initial time step to steady state convergence are shown in Fig. 7.

(a) Comparison of the analytical and graph theory solutions

To compare the accuracy of the graph theory approach with the analytical solution (Fig. 7), we conduct the analysis in three steps as shown in Fig. 8. In this section, we also study the effect of a number of nodes and their connection structure on the convergence accuracy of the approach.

Step 1: Generation of nodes

The whole part is transformed into a set of 91,000 discrete nodes. We randomly sampled a different number of nodes from these 91,000 nodes as shown in Fig. 8 to study the effect of the number of nodes on the accuracy of the graph-theoretic solution. Since the heated volume is one-eighth of the total volume of the cube, we ensure that the number of nodes in the heated subsection is exactly one-eighth of the total number of nodes ($91,000/8 = 11,375$). Each node takes the character of its location, i.e., the nodes which are in the heated subsection take the high-temperature value (equal to 1, which is the highest in normalized temperature range) and the nodes that are outside the heated subsection are set at the low-temperature value (equal to 0, which is the lowest in normalized temperature range) at the initial time step.

Step 2: Network graph construction

In this step, the selected nodes are used to construct a network graph based on their spatial coordinates and neighborhood distance (ϵ), which is stored in the adjacency matrix as described in Sec. 3.2. Based on the total number of selected nodes and analytical diffusion time, a specific neighboring distance (ϵ) is required to set the neighboring area for each node. Each node is connected to approximately 20, 80, 300, and 600 neighboring nodes in cases 1, 2, 3, and 4, respectively, as reported in Table 1.

Selecting a higher number of nodes implies a larger adjacency matrix size and requires longer computational time. The computational time corresponds to converting the part to set of discrete nodes and building adjacency matrix which in this work is implemented on a desktop

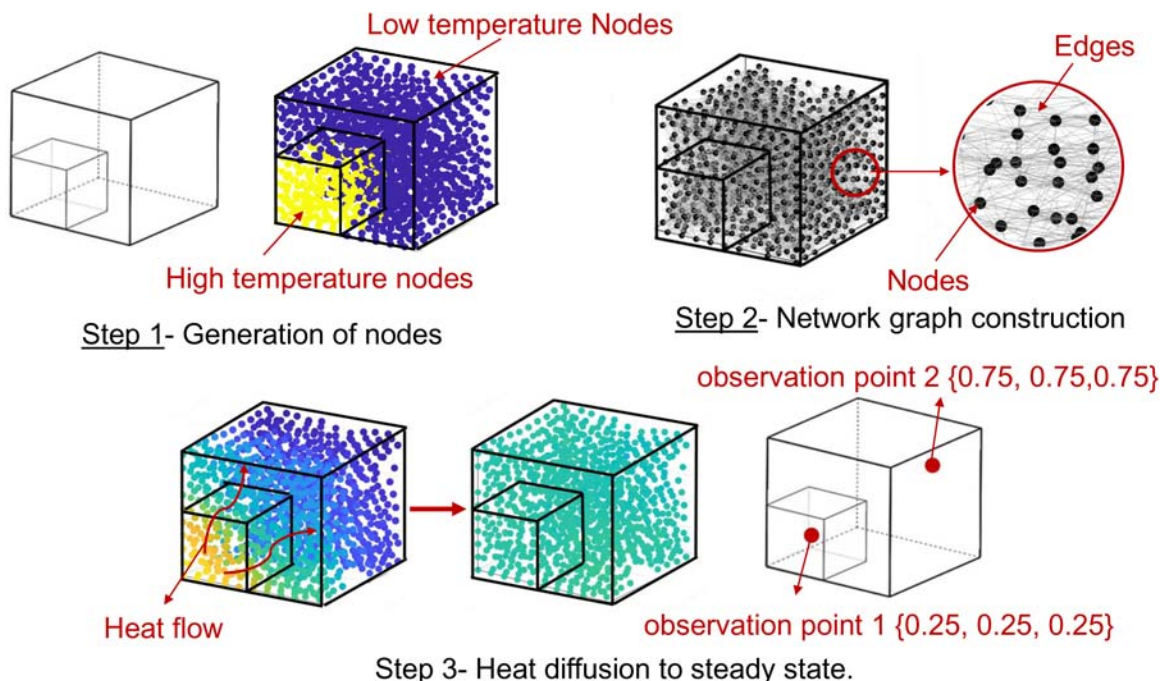


Fig. 8 The three steps toward the error calculation and verification with the analytical method

Table 1 Details of graph theory heat diffusion experiment in a cube (1 × 1 × 1 unit)

Case	Total number of selected nodes (cold:heated)	Neighbourhood distance (ϵ) units	Network graph construction time (s)	Total graph-theoretic solution computational time (s)	SMAPE (error) (%)	RMSE
1	80 (10:70)	0.55	0.94	0.97	10	0.1012
2	800 (100:700)	0.37	1.41	1.55	7	0.1003
3	4000 (500:3500)	0.31	20.78	38.14	5	0.0991
4	8000 (1000:7000)	0.28	163.33	236.64	3	0.0932

computer with an Intel® Core™ i7-6700 CPU @3.40 GHz, 32 GB RAM. Table 1 shows the neighborhood distance (ϵ), adjacency matrix (A) size, and graph construction computational time in each case.

Step 3: Heat diffusion to steady state

The heat diffuses through the graph network until it reaches a steady-state condition. We consider the same two observation points, point 1 at {0.25, 0.25, 0.25} and point 2 at {0.75, 0.75, 0.75}. The steady-state condition is achieved when both observations have the equal temperature up to the fourth decimal point; thermal diffusivity (α), which corresponds the material properties in the graph theory method, was considered to be equal to 1 unit (m^2/s). Figure 9(a) compares the trend of heat diffusion computed using graph theory for case 2 with the analytical solution. The symmetric mean absolute percent error (SMAPE) and root mean square error (RMSE), defined in Eq. (20), are used to quantify the error, where t is the time step and e is the absolute error. Figure 9(b) shows the trends of the SMAPE for the four different cases. Although increasing the number of nodes reduces the error, it leads to a longer computational time.

Table 1 delineates the SMAPE, RMSE, and total computational time of the process based on the different number of nodes, from which it is evident even with the sparsest node condition (80 nodes in a cube of $1 \times 1 \times 1$ unit), the error is less than 10%.

$$\text{SMAPE} = \frac{100\%}{n} \sum_{\forall t} e(t)$$

$$e(t) = \frac{|\text{Analytical solution}(t) - \text{Graph theoretic solution}(t)|}{(\text{Analytical solution}(t) + \text{Graph theoretic solution}(t))} \quad (20)$$

RMSE =

$$\sqrt{\frac{\sum_{t=1}^n (\text{Analytical solution}(t) - \text{Graph theoretic solution}(t))^2}{n}}$$

(b) Comparison of the graph theory and finite element analysis solutions.

Continuing with our study of heat diffusion for the cuboid geometry, we now compare the graph-theoretic and FE analysis solutions. The FE analysis study is implemented in ABAQUS software. The FE analysis process is divided into three steps as shown in Fig. 10.

Step 1: Mesh generation in finite element analysis

We applied both tetrahedral and regular grid (hexahedron) meshes on the cube. It was observed that tetrahedral mesh performs better than regular grid mesh in terms of accuracy.

Step 2: Boundary condition and initial heat condition in finite element analysis

Identical boundary conditions as in the case of the analytical method are applied herewith, i.e., the heat disperses through the part, and the cube is perfectly insulated (Neumann boundary condition). As with the analytical method, the material properties such as thermal conductivity, specific heat, and density of material in this method are considered to be equal to 1 unit.

Step 3: Heat diffusion to steady state in finite element analysis

The heat diffuses through the cube volume until a steady-state condition is reached. Table 2 reports a comparison between the total calculation time and a number of nodes for FE analysis and graph theory. The number of nodes in FE analysis was chosen to give approximately the same error as graph theory. The result shows that the proposed graph-theoretic approach gives comparable accuracy at within a fraction of the computational time taken by FE analysis.

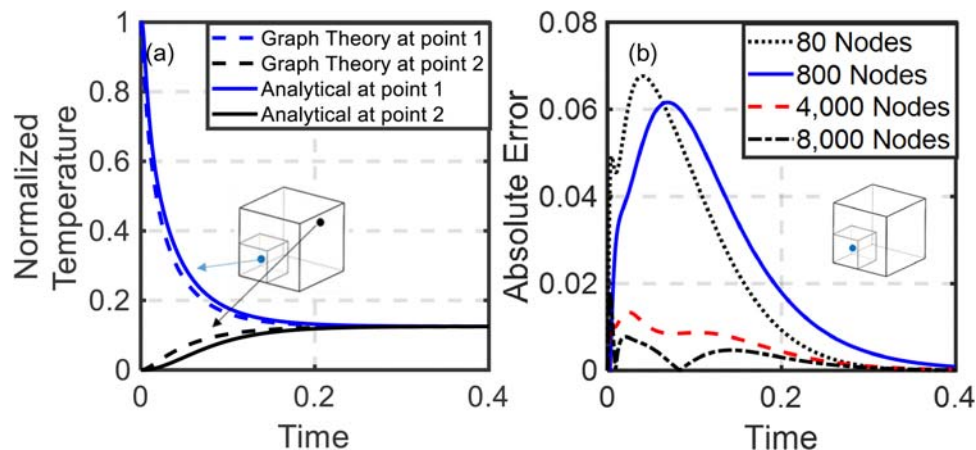


Fig. 9 (a) Comparison of the heat diffusion trend between graph theory and analytical method (result of Case 2 with 800 selected nodes) and (b) absolute error comparison for different amount of nodes at observation point 1

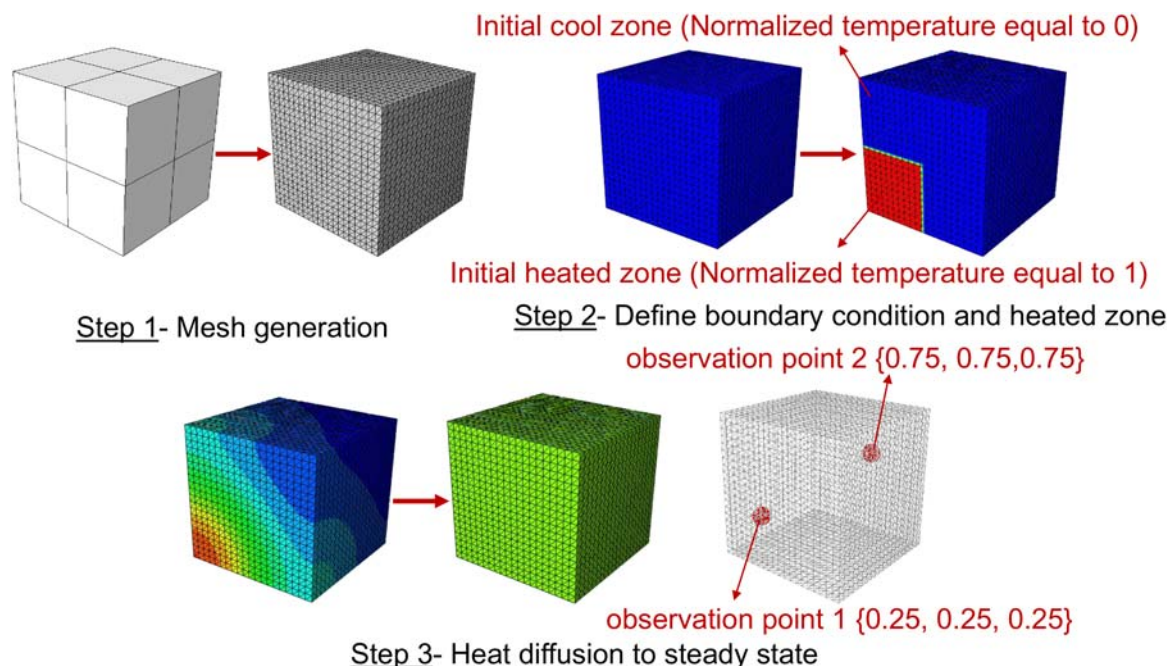


Fig. 10 The three steps of FEA toward the error calculation and verification with the analytical method

Table 2 Comparison of FEA and graph-theoretic approach based on the total computational time and accuracy

SMAPE (error) (%)	Graph-theoretic approach		Tetrahedral FE analysis		Regular grid FE analysis	
	Nodes	Time (s)	Nodes	Time (s)	Nodes	Time (s)
10	80	1	1200	190	9000	380
7	800	2	12,000	660	158,500	9000
~5	8000	237	76,000	3540	1,000,000	43,000

4.2 Verification of the Graph Theory Approach With Goldak's Finite Element Analysis Solution in LPBF

- (a) Finite element analysis of LPBF parts based on Goldak's moving heat source model.

We now compare the solutions resulting from the graph-theoretic approach with FE analysis for three test objects in the LPBF scenario using Goldak's model. Goldak et al. extended the pioneering work of Rosenthal [68] to predict the temperature distribution in the welding process [64,65]. Goldak et al. considered a 3D moving heat source model with an ellipsoidal, Gaussian density distribution as opposed to Rosenthal's 1D moving point heat source.

Goldak's model has been adapted for thermal modeling in the AM process, e.g., in LPBF with the laser considered a 3D Gaussian distributed moving heat source [69]. We use Goldak's model in an FE analysis framework (ABAQUS) with an element birth-and-death technique to simulate the LPBF process; the DFLUX subroutine in ABAQUS is leveraged to model the characteristics of the laser. The Gaussian distributed laser heat source is written as

$$Q(x, y, z) = \frac{PA}{2\pi\sigma^2} e^{-(d^2/2\sigma^2)} \quad (21)$$

where Q is the volume heat power density (W/mm^3), P is the laser power (W), A is the constant of absorptivity set to 0.7, σ is the standard deviation (quarter of the beam diameter in meters), and d (m) is the radial distance of a point from the

center of the beam [70]. The term Q is identical to the energy density term E_v in Eq. (1). The simplest form of the transient heat conduction, identical to Eq. (1), is used in this study, with E_v set equal to Q . In this mode, conduction plays the main role in transferring the applied heat through the part and substrate. The radiative heat losses are not considered in this study to make an equitable comparison with the graph-theoretic approach.

- (b) Description of the boundary conditions and test part geometries.

The LPBF of two C-shaped test parts (Figs. 11(a) and 11(b)) and a pyramid-shaped test part (Fig. 11(c)) are simulated (separately, one at a time) on top of a build plate with the dimension of $100 \times 20 \times 10$ mm having identical material as the test parts (Titanium alloy Ti6Al4V). The C-shaped part in Fig. 11(a) has an overhang geometry akin to the knee implant in Fig. 3. The second C-shaped part, Fig. 11(b), has the overhang area provided with thick supports. Figure 12 shows the scanning strategy used for these parts in the LPBF simulation. The hatches (the linear scan pattern of the laser) are defined along the y -axis and layers along the z -axis.

The laser is simulated to move along the x -axis and traces a linear hatch pattern in each layer. Based on the width of each layer, the number of hatches per layer remains constant in the two C-shaped parts but vary in the pyramid test part, i.e., 20 hatches in the first layer, 18 hatches in the second layer, and so on, until finally only one hatch is needed in layer 20. The hatch spacing and layer thickness are 0.5 mm and 0.2 mm for the two C-shaped parts, and pyramid, respectively.

The layer thickness is purposely made exceedingly coarse to facilitate computation and should ideally be termed as a super layer—each super layer consists of 20 individual layers of size 0.025 mm (25 μm) for the C-shaped parts and 8 super layers for the pyramid part. These super layers are consolidated in an identical manner for the finite element and proposed graph-theoretic approach. The titanium alloy powder material Ti6Al4V is considered for both the part and the build plate. The material properties and printing conditions are reported in Table 3, based on the literature [66,69].

The parameters for the graph-theoretic approach were set as follows: neighborhood size $\varepsilon = 2$ mm; gain factor $g = 2.2 \times$

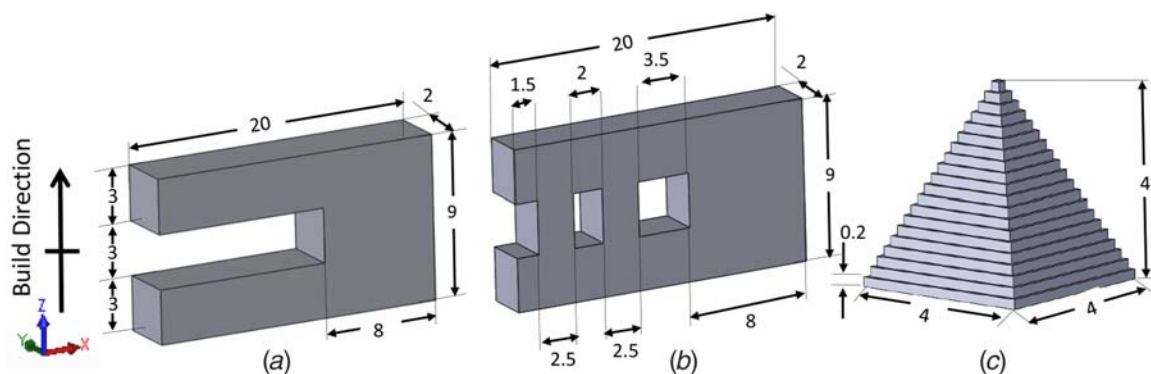


Fig. 11 (a) C-shaped, (b) C-shaped with support, and (c) pyramid dimensions in millimeters

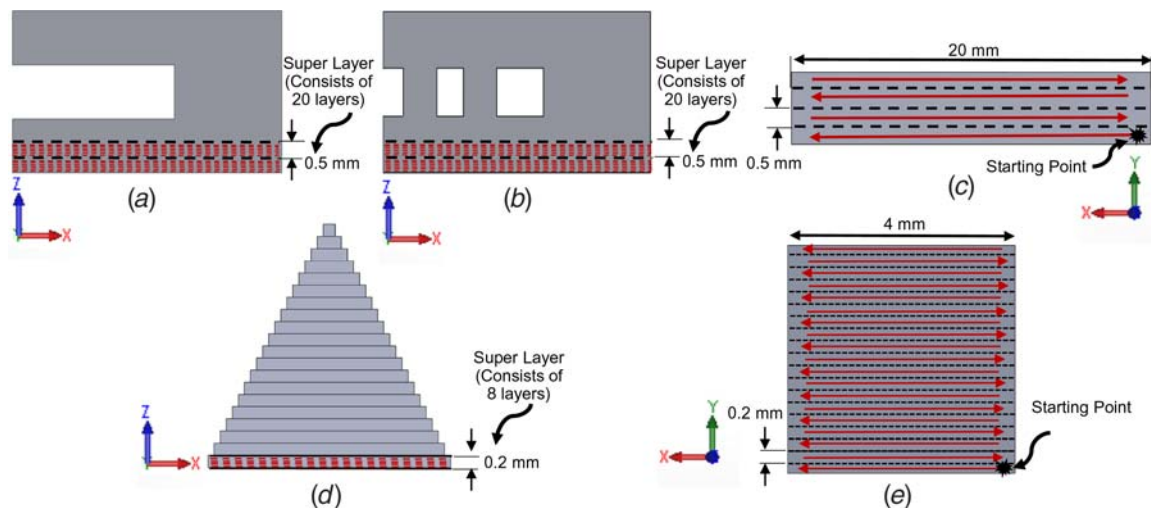


Fig. 12 (a) Side view of C-shaped part, (b) side view of C-shaped part with supports, (c) scanning strategy of the two C-shaped parts from top view, (d) side view of pyramid part, and (e) scanning strategy of pyramid part from its top view

Table 3 Materials and process parameters for the FE analysis (ABAQUS) and NETFABB simulation

Parameters	Values	
	C-shaped parts	Pyramid
Layer thickness (mm)	0.025	
Super layer thickness (mm)	0.5 (20 layers)	0.2 (8 layers)
Hatch thickness (mm)	0.5	0.2
Beam diameter (mm)	0.5	0.2
Laser power, P (W)	200	
Scanning speed (mm s^{-1})	200	
Thermal conductivity, k ($\text{W m}^{-1} \text{K}^{-1}$)	20	
Thermal absorptivity coefficient, A	0.7	
Thermal diffusivity, α ($\text{m}^2 \text{s}^{-1}$)	7×10^{-6}	
Material density, ρ (kg m^{-3})	4300	
Specific heat, C_p ($\text{J kg}^{-1} \text{K}^{-1}$)	650	
Ambient temperature, T_∞ (K)	298	

10^6 m^{-2} and various levels of nodes density are sampled per hatch in the C-shaped parts with supports, with the optimal level recommended as 80 nodes per hatch. These parameters for the pyramid are $\varepsilon = 0.25 \text{ mm}$, $g = 2.2 \times 10^6 \text{ m}^{-2}$, and 40 nodes are sampled per hatch. The justification and guidelines for the selection of these parameters are tendered within Sec. 4.2(b). The temperature history at three locations on the bottom for the C-shaped part and one location on the

bottom for the pyramid were recorded over the complete simulation run, analogous to the presence of thermocouple sensors affixed to the part at these locations.

- (c) Temperature distribution in a C-shaped part without supports.

For both the C-shaped parts, the temperature history is observed at three locations, akin to embedding a thermocouple sensor as demarcated in the inset of Fig. 13. The observation points (sensor locations) are (1) at a distance of 1 mm from the left edge; (2) 1 mm from the right edge of the part; and (3) in the center of the part 10 mm away from either edge. The observation locations are located 0.5 mm from the bottom of the part and 1 mm deep from the front edge of the part.

Furthermore, we also report the result of adjusting the number of nodes at three discrete levels of (a) 20 nodes per hatch (1440 total nodes); (b) 80 nodes per hatch (5760 total); and (c) 120 nodes per hatch (8640 total). We observe from Fig. 13 that the temperature trends predicted by the graph-based approach mimics the corresponding trends obtained from FE analysis, and the correlation between the two trends improves as the number of nodes is increased. As reported in Table 4, the SMAPE for the graph-based approach (20 nodes per hatch) with FE analysis taken as the ground truth is less than 20%; the error reduces to less than 10% when 120 nodes are sampled per hatch.

From a computational efficiency perspective, as reported in Table 4, the simulation time of C-shaped part for the FE

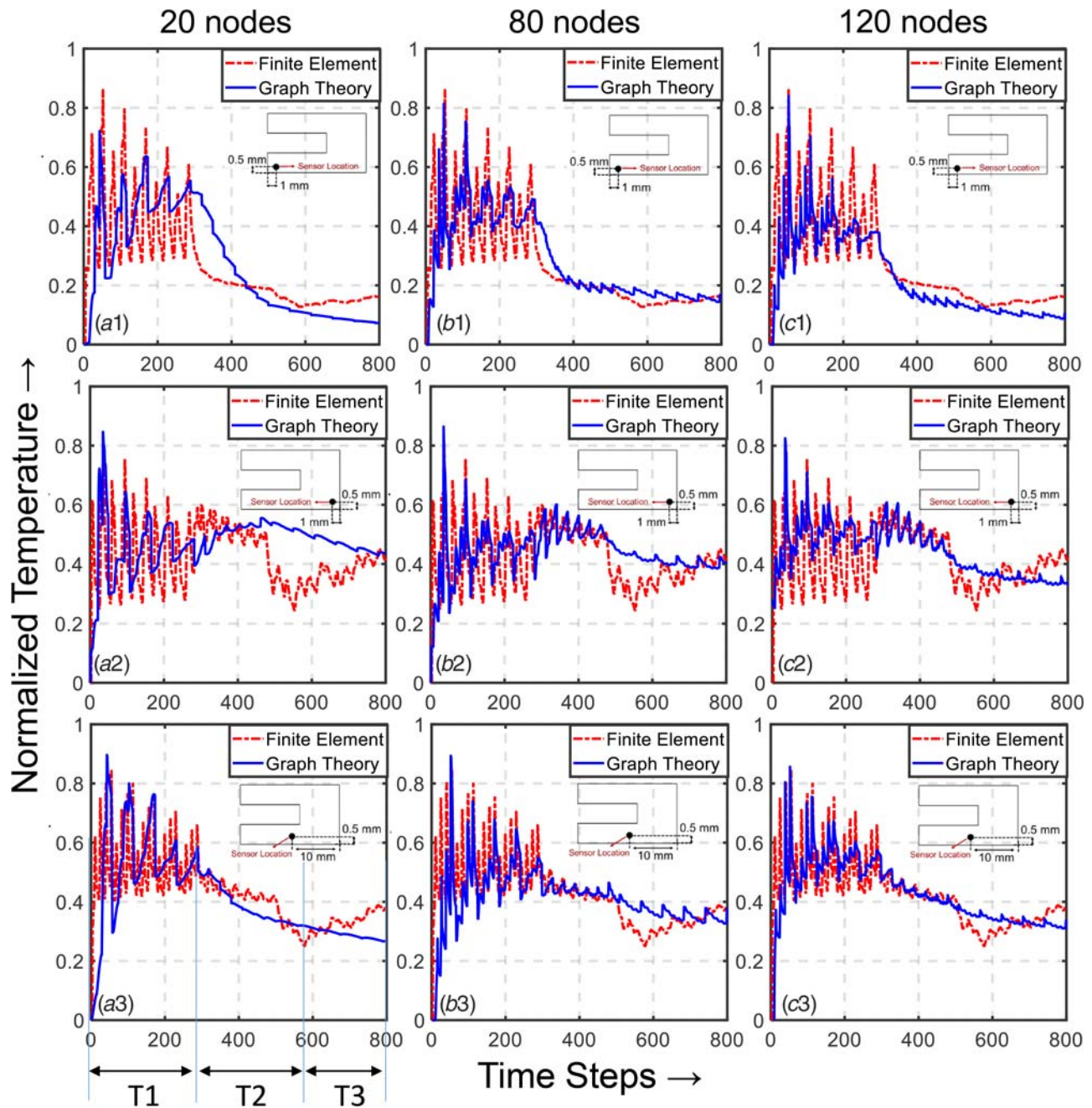


Fig. 13 (a) The C-shaped part and the normalized temperature trends observed at three locations on the part: (1) in the bottom left, (2) bottom center, and (3) center, respectively, corresponding to three node densities per hatch: (a) 20, (b) 80, and (c) 120 nodes. The neighborhood size is $\varepsilon = 2$ mm and the gain factor is set at $g = 2.2 \times 10^6$.

approach (on ABAQUS) was close to 200 min (>3 h) on a dual core of Intel® Core™ i7-6700 CPU @3.40 GHz, 32 GB RAM. While the computation time for the graph-theoretic approach was less than 30 s (0.5 min) on the same machine with MATLAB considering 20 nodes per hatch and close to 2460 s (41 min) with 120 nodes per hatch.

The temperature trends, particularly the sharp temperature peaks (spikes), observed in the C-shaped part is explained in the context of the observation point located in the center of the part with 80 nodes per hatch, i.e., Fig. 13(b3). The trends reported in Fig. 13(b3) are analyzed in-depth by partitioning the part geometry into three sections T1, T2, and T3 as demarcated in Fig. 14(a). Fig. 14(a) shows the laser scan path (hatch pattern). The spikes in section T1 in Figs. 14(b) and 14(c) correspond to the locations where the laser

is in close vicinity of the observation point, i.e., directly (in the vertical direction) above or in-plane. In section T2, the laser no longer passes over the location of the observation point leading to the observed precipitous drop. In section T3, given the impeded conductivity of the powder surrounding the overhang, the sensor location temperature does not increase, though the laser does pass directly over the sensor location. Figure 14(c) shows the four peaks corresponding to the four instances where the laser is in close proximity to the measurement point.

We once again note the ability of the graph-based approach to mimic, not only the overall trends predicted with FE analysis but also the match temporally the temperature spikes caused by the hatch pattern of the laser. The effect of nodes on the approach is further explained from Fig. 13.

Table 4 Comparison of calculation time and SMAPE for FE analysis (ABAQUS) and graph theory solutions for the three test parts

Part	Result	Number of nodes in a hatch (total)	SMAPE (percent. error) (%)	RMSE	Computation time (min) with graph-based approach	Computation time (min) with FE analysis (ABAQUS)
C-shaped part without supports	Figure 13(a1)	20 (1440)	18.9	0.125	0.5	≈200 (2880 elements)
Left side observation point	Figure 13(b1)	80 (5760)	11.2	0.103	18	
C-shaped part without supports	Figure 13(c1)	120 (8640)	9.9	0.095	41	
Right side observation point	Figure 13(a2)	20 (1440)	15.6	0.133	0.5	
C-shaped part without supports	Figure 13(b2)	80 (5760)	9.2	0.105	18	
Right side observation point	Figure 13(c2)	120 (8640)	8.8	0.097	41	
Center observation point	Figure 13(a3)	20 (1440)	11.3	0.111	0.5	
C-shaped part without supports	Figure 13(b3)	80 (5760)	7.5	0.094	18	
Center observation point	Figure 13(c3)	120 (8640)	5.7	0.076	41	
C-shaped part with supports	Figure 19(a)	80 (5760)	10.1	0.091	18	≈208 (3390 elements)
Left side observation point	Figure 19(b)	80 (5760)	10.7	0.096		
C-shaped part with supports	Figure 19(c)	80 (5760)	7.8	0.084		
Right side observation point						
C-shaped part with supports						
Center side observation point						
Pyramid	Figure 20	40 (8000)	6.7	0.068	66	≈1380 (24,000 elements)

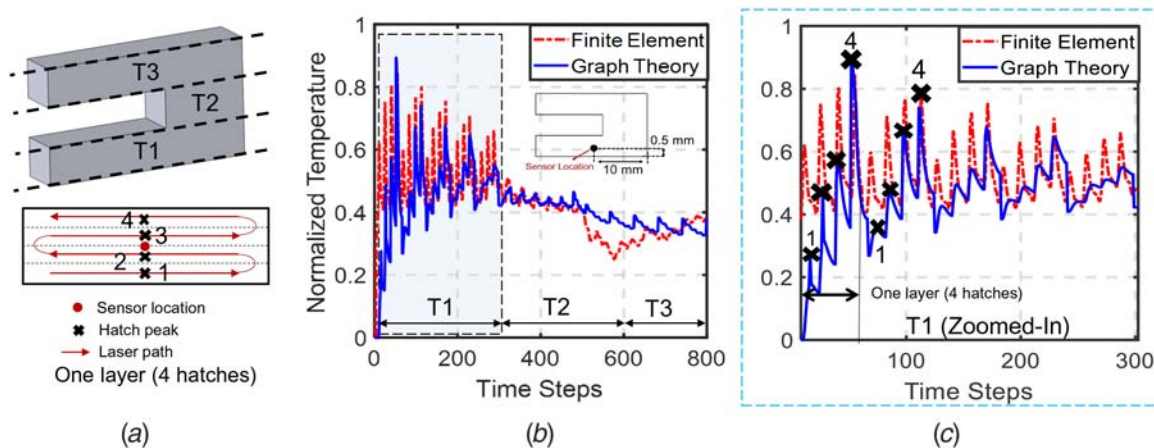


Fig. 14 Explanation for the temperature trends and spikes observed at the center location. (a) The hatch demarcation of the part into three sections, and hatch pattern simulated, (b) the temperature trends observed at the bottom center, and (c) zoomed in view of section T1, noting that the temperature spikes correspond to the spatiotemporal location of the laser in relation to the observation point (sensor location) demarcated in (a). The neighborhood size is $\epsilon = 2$ mm and the number of nodes per hatch is held constant at 80, and the gain factor is set at $g = 2.2 \times 10^6$.

When the number of nodes in a hatch is greater, e.g., 80 or 120, the graph-based approach captures the temperature spikes in each layer corresponding to each hatch; with a lower number of nodes, namely, 20 the individual spikes corresponding to a hatch are smoothened.

In a similar vein, referring to Fig. 13(b2), for the bottom right sensor, the spikes in section T1 of the part correspond to the location where the laser passes over the measurement point on the right. In area T2, the increase in temperature compared with the center sensor discussed above can be attributed to two reasons: (i) in section T2 of the part, the laser passes frequently and directly above the location of the observation point and (ii) section T2 is surrounded by a large volume of powder around it that hinders the flow of heat through it to the substrate.

(d) Procedure for calibration of the gain factor (g) and neighborhood distance (ϵ) parameters.

(i) Effect of gain factor.

To measure the effect of gain factor on the graph theory-based approach, we simulated 40 different gain factor values in the context of the temperature trends observed in the central observation point for the first three layers of section T1 of the C-shaped part (Fig. 14 (b)). As in previous cases, both the RMSE and SMAPE, are used to evaluate the difference between the normalized temperature trends obtained from graph theory approach and the finite element method (ABAQUS) as a baseline reference. The results are reported in Fig. 15, which shows that for this particular case, the gain factor value, $g = 2.2 \times 10^6$, results in the smallest RMSE and

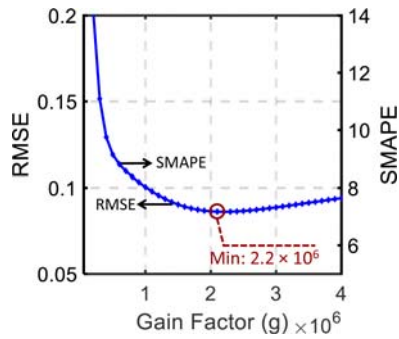


Fig. 15 Effect of gain factor on the RMSE and SMAPE in simulating three layers of section T1 from the C-shaped part. The neighborhood size is $\varepsilon = 2$ mm and the number of nodes per hatch is held constant at 40.

SMAPE and corresponds to the best match of the graph theory model with the finite element analysis results. We reiterate that this gain factor value $g = 2.2 \times 10^6$ has been used throughout in case of all the three tests part reported in this section, viz., C-shape part without supports, C-shape part with supports, and pyramid (Fig. 11).

The physical significance of the gain factor is explained with reference to Fig. 16, which shows the temperature trends observed at the center location of the first three layers of the C-shaped part with 40 nodes per hatch (first three layers in Fig. 14(c)). Figure 16 leads to the

insight that the gain factor governs the rate of heat diffusion; a smaller gain factor will impede the rate of heat diffusion, while higher gain factor values amplify the same.

As a result of an increase in the gain factor, the temperature fluctuations closely track the periodic thermal patterns resulting from hatch-by-hatch fusion (as depicted formerly in Fig. 14(c)). However, an inordinately high gain factor will lead to faster decay in temperature, and thereby result in temperature that falls below the FE solution. There are two practical approaches to choose the gain factor for the graph-based approach, the first is to use the analytical solution as a ground truth, and the second is to simulate a small section of a part with FE methods and use the FE results as a baseline to adjust the gain factor, as done in this study.

(ii) Effect of neighborhood distance (ε).

Choosing an appropriate neighborhood distance inherently involves (a) a tradeoff between computational effort and accuracy and (b) the physical geometry of the part.

Based on the evidence presented in Fig. 17, we suggest the following general guidelines:

- Neighborhood distance (ε) should be smaller than the characteristic length of the part. The characteristic length of a part is dictated by the geometry and is the distance beyond which there should not be any physical connection between nodes. For example, in C-shaped part nodes from overhang section (T3) and first tier (T1) should not be considered as directly connected, because it would entail crossing the boundary

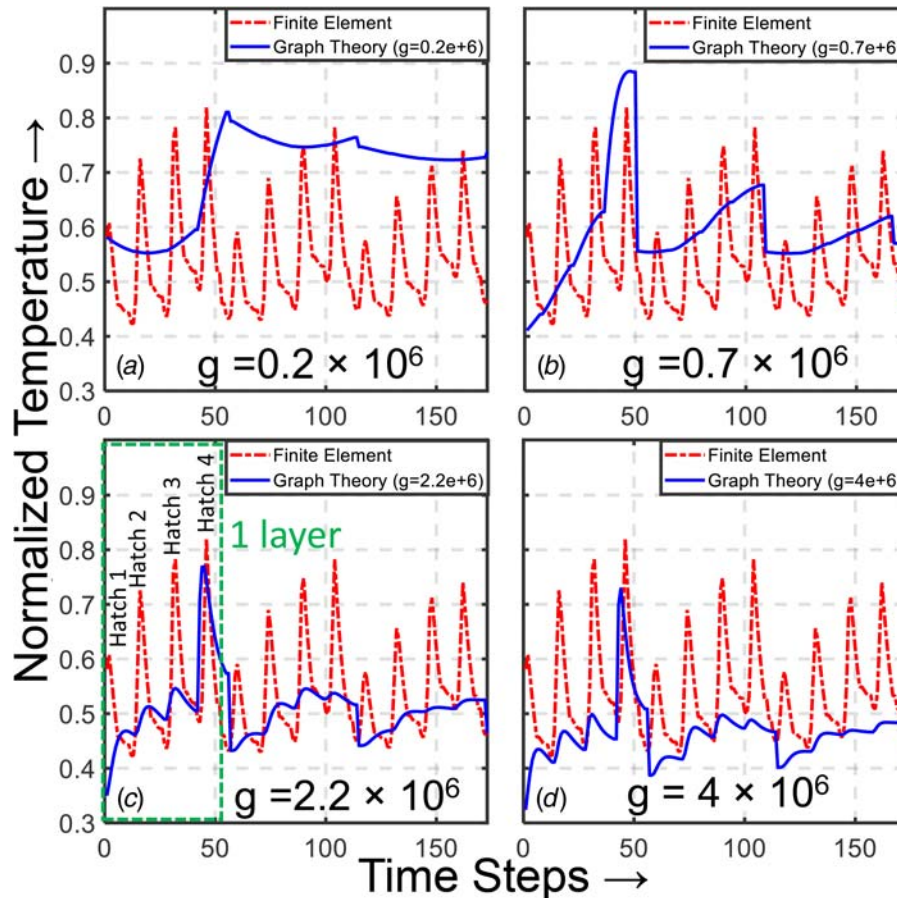


Fig. 16 The effect of gain factor (g) on the thermal trends observed in the center of the first three layers of the C-shaped part with 40 nodes per hatch and neighborhood distance $\varepsilon = 2$ mm. At lower gain factor (a) $g = 0.2 \times 10^6$ and (b) $g = 0.7 \times 10^6$, the rate of heat diffusion (heat flux) is restrained, as the gain factor is increased to (c) $g = 2.2 \times 10^6$ and (d) $g = 4 \times 10^6$ the rate of diffusion is comparatively faster.

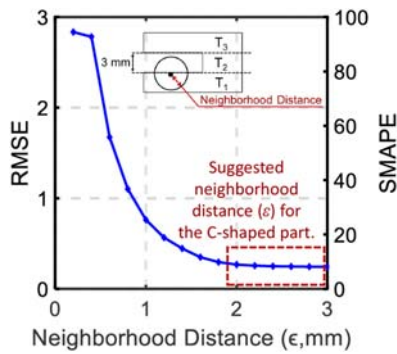


Fig. 17 The effect of neighborhood distance (ϵ) on the RMSE and SMAPE in simulating three layers of section T1 from the C-shaped part. A neighborhood distance between 2 mm and 3 mm is suggested given the characteristic length of the part.

separating the part edges and the surrounding powder. So the distance from T3 to T1, which is 3 mm, is the characteristic length of the C-shaped part.

- For a given node density, a smaller neighborhood distance means that each node is connected to fewer neighbors. As the number of nodes connected

becomes smaller, the heat transfer between the nodes are not captured with sufficient accuracy and the temperature variations are smaller.

Figure 17 shows the effect of the neighborhood distance on the graph theory simulation for the C-shaped part. Beyond neighborhood distance $\epsilon = 2$ mm, the RMSE and SMAPE reaches a minimum, beyond $\epsilon = 3$ mm executing the simulation is no longer physically viable as it exceeds the characteristic length, and for $\epsilon < 2$ mm the error is high because the connectivity of the nodes is sparse; each node is connected to so few of other nodes that the heat transfer phenomena are not captured, consequently, the trends are smoothed. At higher values of the neighborhood distance, the accuracy of the graph-theoretic solution increases, vis-à-vis the FE solution; however, the computational burden increases exponentially (n nodes require $n(n-1)$ edges to be computed) with vanishing decrease in the error. In this work, we chose $\epsilon = 2$ to balance between accuracy and computational efficiency.

The effect of the neighborhood distance on the thermal trends obtained from the graph theory approach is further examined in Fig. 18, which tracks the normalized temperature at the center observation

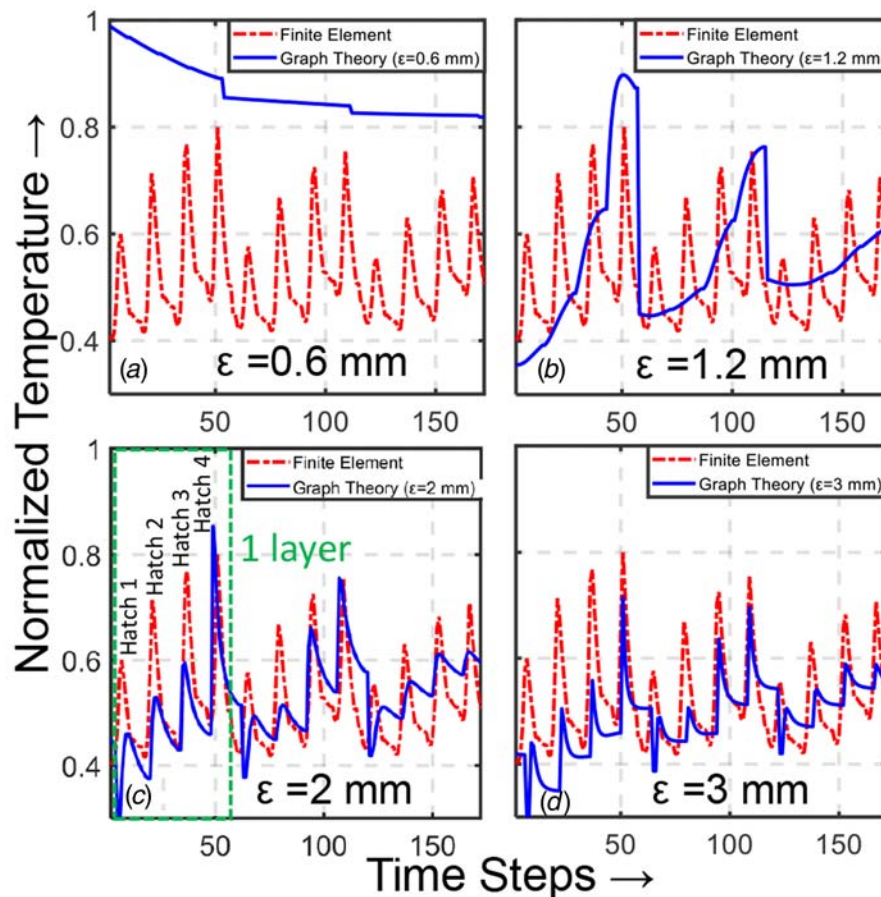


Fig. 18 The effect of the neighborhood distance (ϵ) on the thermal trends observed in the first three layers of the C-shaped part when compared with the FE solution. The number of nodes per hatch is set at 80, and gain factor $g = 2.2 \times 10^6$. At lower values of neighborhood distance (a) $\epsilon = 0.6$ mm and (b) $\epsilon = 1.2$ mm, the number of nodes is too sparse to capture the heat transfer phenomena. At larger values of the neighborhood distance of (c) $\epsilon = 2$ mm and (d) $\epsilon = 3$ mm, the individual spokes in a layer are matched temporally with the FE solution; however, the computation time increases exponentially, as the number of nodes connected are larger.

point for the first three layers of the C-shaped part with 80 nodes per hatch (first three layers in Fig. 14(c)). At lower neighborhood distances of $\varepsilon = 0.6$ mm and 1.2 mm, there are a sparse number of nodes that are within a sphere of radius ε , consequently, there are a few number of edges connecting the nodes, and hence, the heat transfer amongst them is ill represented. The fidelity of the simulation increases considerably at $\varepsilon = 2$ mm.

(e) Temperature distribution in a C-shaped part with supports.

Based on the temperature distribution results from the C-shaped part (Fig. 13) which showed that the heat tends to be constrained in the overhang section. It was also hypothesized that designing supports (under the overhang) would provide a pathway for the heat to dissipate into the build plate. Accordingly, the C-shaped part was modified as shown in Fig. 11(b). We note that the cross section of the support is designed with the same thickness as the rest of the part. The build process was simulated using identical settings for the FE analysis and graph-theoretic approach (Fig. 12).

Identical to the previous case with the C-shaped part without supports described in Sec. 4.2(b), the temperature trends for the C-shaped part with supports are observed at the three locations, namely, left, right, and center at 0.5 mm from the bottom of the part. The graph theory-based simulation is implemented with 80 nodes sampled per hatch (5760 nodes total). The trends predicted using FE analysis and graph theory are overlaid in Fig. 19 for each of the observation points, which shows that the trends obtained with the graph-

based approach match temporally with those from FE analysis. Further, as evident from Table 4, the SMAPE ranges from $\approx 8\%$ to 11%. The simulation is completed within 20 min with graph theory, as opposed to over 200 min with FE analysis.

Further, juxtaposing Figs. 19(a)–19(c) against, Figs. 13(c1)–13(c3), respectively, it is evident that placing the supports under the overhang section aids in the dissipation of heat. For instance, in Fig. 19(a), the temperature reduction at the end of section T1 is not precipitous as in Fig. 13(c1). Therefore, the possibility of thermal stress-related deformation and cracking are potentially minimized. Further, this result can lead to an understanding of the impact of supports on the magnitude and direction of the heat flow (heat flux), and thus opens a path to the use supports as a design feature to not only to anchor the part but also as a means to conduct the heat trapped in a narrow area, such as an overhang.

(f) Temperature distribution in a pyramid-shaped part.

Figure 20 delineates the temperature history at a measurement point which is located in layer 3 for the pyramid-shaped part. Each spike in Fig. 20 corresponds to the layer in which the laser passes over the measurement point. The height of spikes becomes ever smaller as the laser moves to the subsequent layers, due to proportionally smaller energy applied per layer, and also because the bottom layers have a larger area, which facilitates heat dissipation.

(g) Comparison of temperature history and temperature distribution results from finite element analysis (ABAQUS) and a commercial software (NETFABB) with graph-theoretic solution

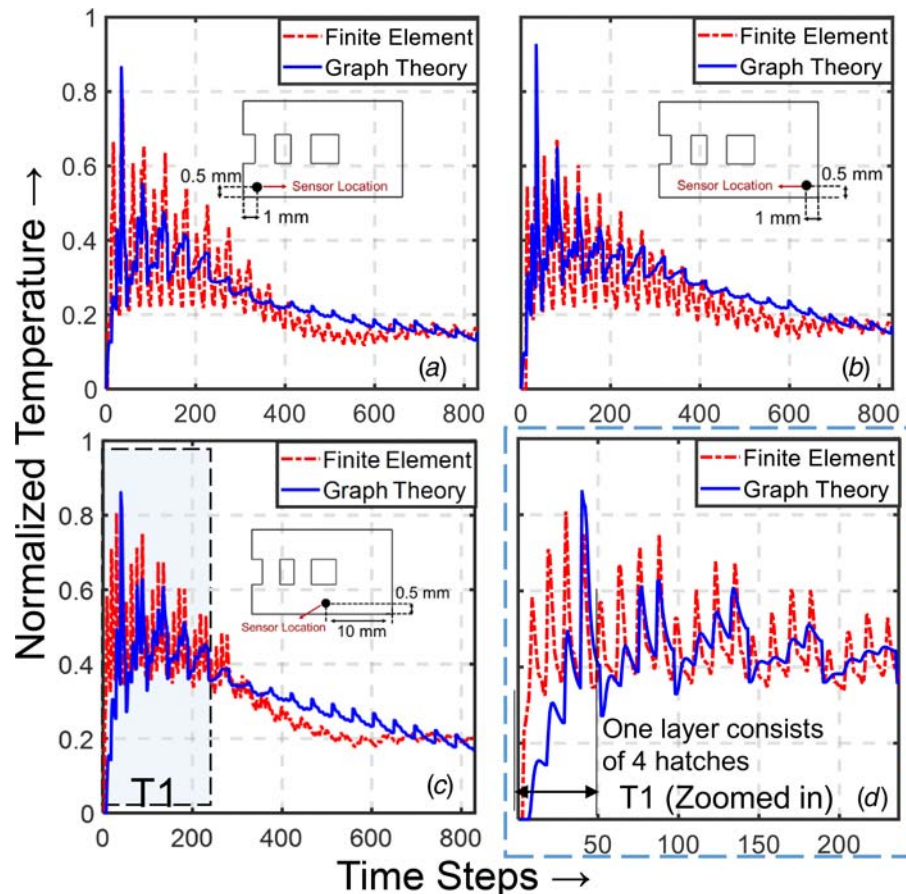


Fig. 19 The C-shaped part from Fig. 13 is modified with two supports to provide a path for the heat in the overhang section to dissipate. The temperature trends observed at three locations on the part, in (a) left, (b) right, and (c) center. A zoomed in plot corresponding to the section T1 from (c) is shown in (d). The neighborhood size is $\varepsilon = 2$ mm and the number of nodes per hatch is held constant at 80, and the gain factor is set at $g = 2.2 \times 10^6$.

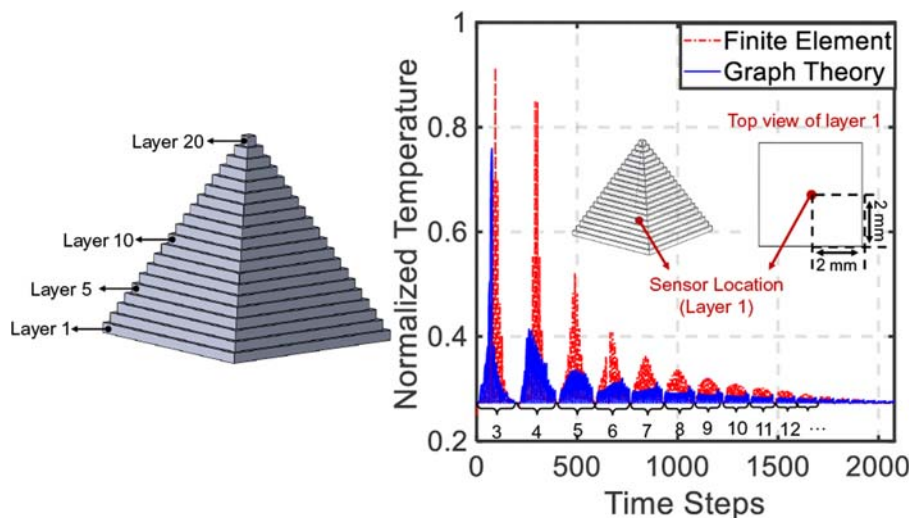


Fig. 20 The temperature profile for an observation point located at the center of layer one, and 40 nodes per hatch, and neighborhood distance $\varepsilon = 0.25$ mm, and gain factor g set at 2.2×10^6

The computation time and error (SMAPE, Eq. (20)) between the thermal trends obtained from the graph theory and FE methods for the three parts are reported in Table 4. These results indicate that the thermal trends predicted by the graph theory and FE-based approaches are within $\approx 10\%$ when a sufficiently large node density is chosen (80 or 120 nodes per hatch). More pertinently, the computation time with graph theory is a fraction of that taken by FE

analysis. In our forthcoming research, we will attempt to further improve this result by including thermal phenomena, such as radiative effects, ignored in this work.

Lastly, the temperature distribution results from the last layer of Goldaks's FE model, solution from the commercial NETFABB's package, and graph-theoretic simulations are juxtaposed pictorially in Fig. 21. The scale bars represent normalized temperature between 0 and 1. From Fig. 21, it is

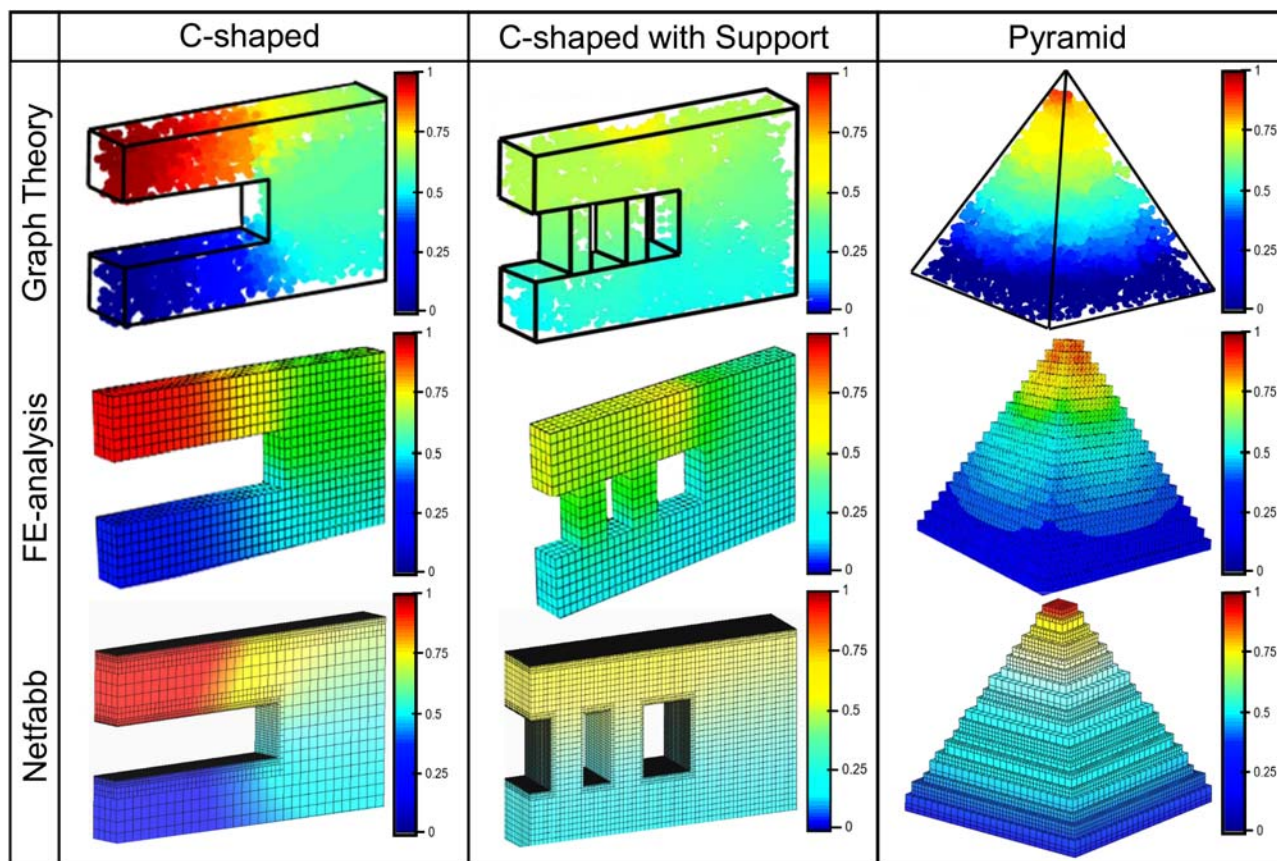


Fig. 21 Temperature distribution of three parts which is compared by three different methods; graph theory (50 nodes per hatch), FE analysis (ABAQUS), and commercial software (NETFABB)

evident that the temperature distribution captured by the graph-theoretic approach closely resembles those derived from the Goldak's FE model and Autodesk's NETFABB. We note that in Fig. 21, an entire vertical plane of the C-shaped part without supports is at an elevated temperature because the heat accumulates in the overhang section due to the insulating nature of the surrounding powder.

In closing this section, we reemphasize that the main advantage of the graph theory-based approach is that it solves a discrete approximation Eq. (3) of the continuum heat diffusion equation, Eq. (2). This discretization of the part geometry, which takes the form of point nodes in the graph theory approach as opposed to uniform volumetric elements as done in conventional mesh-based FE analysis facilitates magnitude faster prediction of temperature history in metal AM parts. To explain further, the solution to the discrete heat equation, Eq. (3), from the graph theory-based approach requires eigen decomposition of a matrix, whereas in FE analysis the continuum heat equation (Eq. (2)) is solved computationally for each element. The case studies detailed in Secs. 4.2(b)–4.2(d) and summarized in Table 4 affirm the assertion that graph theory simulation can reduce the computational time to one-tenth of FE analysis implemented in the context of Goldak's model applied to metal AM, while maintaining accuracy within 10%.

Nevertheless, the faster computation enabled by graph theory comes at the cost of discrepancies in the thermal trends at the individual hatch-level. The discrepancy between the FE and the graph-based solutions is most likely due to the energy source-related assumption delineated in Sec. 3.1—the graph-based approach does not consider the shape of the laser beam and only samples a sparse volume of the part in the form of nodes. The fast approximation of temperature history enabled by the graph-based approach presented herein will be leveraged in our future works to reduce the computational burden in predicting part distortion resulting from residual stress.

5 Conclusions and Avenues for Future Work

In this work, we developed and applied a novel graph theory-based approach to predict the instantaneous spatiotemporal distribution of temperature, also called temperature field or thermal history, in metal parts as they are being printed layer-upon-layer using AM processes, such as LPBF. The approach relies on converting a part geometry into discrete nodes and connecting them to form a network graph, and subsequently studying the heat diffusion behavior over the network graph embedded in the part.

The key result of this work is that the eigenvectors (Φ) and eigenvalues (Λ) derived from Laplacian (L) of the network graph solve a discrete counterpart of the continuum heat diffusion equation, which governs the temperature history in AM processes. Simulations of an LPBF process are compared with FE analysis moving heat source model based on the work of Goldak and Akhlaghi [64] and Goldak et al. [65]. More specifically, the discrete approximation of the thermal trends obtained using the graph Laplacian eigenvectors and eigenvalues is observed to closely agree with results from the FE-based approach implementing Goldak's model. The computation time to estimate the temperature distribution with the graph-theoretic approach for the three test parts studied was significantly faster compared with FE approach (ABAQUS). For instance, for a C-shaped part, the simulation time was 18 min using the graph-theoretic approach compared with over 3 hours with FE analysis. The error in the FE and graph-theoretic solutions for the same part was within 10%.

Furthermore, the graph-based results were further compared qualitatively with Autodesk NETFABB solution and showed a similar spatial thermal distribution. While this work presents the first foray into using graph theory for modeling the part-level thermal phenomena in metal AM, the approach remains to be

validated with experimental in-situ temperature measurements. The experimental validation of the approach is also essential to crosscheck the parameters, such as neighborhood distance (ϵ) and gain factor (g) in Eqs. (6) and (13), respectively.

In our forthcoming works in this area, we will also endeavor to answer the following questions:

- What is the accuracy of the temperature trends predicted using graph theory with experimental metal AM data?
- What is the effect of the process conditions, such as laser power, velocity, and scan strategy on the temperature distribution, part deformation, and microstructural evolution in metal AM parts?
- What is the true temperature instead of the normalized temperature? What experimental strategy should be used to calibrate the adjustable parameters, ϵ and g ?

Acknowledgment

One of the authors (PKR) thanks the NSF for funding his research through the following grants CMMI-1719388, CMMI-1739696, and CMMI-1752069 (CAREER) at University of Nebraska-Lincoln. Specifically, the concept of using spectral graph theory for modeling in metal additive manufacturing applications was funded through CMMI-1752069 toward a *correct-as-you-build* smart additive manufacturing paradigm. The authors additionally thank Autodesk for providing complimentary educational licenses for the NETFABB simulation program. The help of Mr. Aniruddha Gaikwad in coding the approach in MATLAB is gratefully acknowledged by the authors.

References

- [1] Schmidt, M., Merklein, M., Bourell, D., Dimitrov, D., Hausotte, T., Wegener, K., Overmeyer, L., Vollertsen, F., and Levy, G. N., 2017, "Laser Based Additive Manufacturing in Industry and Academia," *CIRP Ann.*, **66**(2), pp. 561–583.
- [2] Gibson, I., Rosen, D. W., and Stucker, B., 2010, *Additive Manufacturing Technologies: Rapid Prototyping to Direct Digital Manufacturing*, Springer, Berlin.
- [3] Tofail, S. A. M., Koumoulos, E. P., Bandyopadhyay, A., Bose, S., O'Donoghue, L., and Charitidis, C., 2018, "Additive Manufacturing: Scientific and Technological Challenges, Market Uptake and Opportunities," *Mater. Today*, **21**(1), pp. 22–37.
- [4] Khoda, B., Benny, T., Rao, P. K., Sealy, M. P., and Zhou, C., 2017, "Applications of Laser-Based Additive Manufacturing," *Laser-Based Additive Manufacturing of Metal Parts*, CRC Press, Boca Raton, FL, pp. 253–298.
- [5] Badiru, A. B., Valencia, V. V., and Liu, D., 2017, *Additive Manufacturing Handbook: Product Development for the Defense Industry*, CRC Press, Boca Raton, FL.
- [6] Bauereiß, A., Scharowsky, T., and Körner, C., 2014, "Defect Generation and Propagation Mechanism During Additive Manufacturing by Selective Beam Melting," *J. Mater. Process. Technol.*, **214**(11), pp. 2522–2528.
- [7] Liu, Q. C., Elambasseril, J., Sun, S. J., Leary, M., Brandt, M., and Sharp, P. K., 2014, "The Effect of Manufacturing Defects on the Fatigue Behaviour of Ti-6Al-4V Specimens Fabricated Using Selective Laser Melting," *Proceedings of the Advanced Materials Research*, Melbourne, Australia, Mar. 2–7, pp. 1519–1524. Trans Tech Publications.
- [8] Gorelik, M., 2017, "Additive Manufacturing in the Context of Structural Integrity," *Int. J. Fatigue*, **94**(Part 2), pp. 168–177.
- [9] Seifi, M., Gorelik, M., Waller, J., Hrabec, N., Shamsaei, N., Daniewicz, S., and Lewandowski, J. J., 2017, "Progress Towards Metal Additive Manufacturing Standardization to Support Qualification and Certification," *JOM*, **69**(3), pp. 439–455.
- [10] Lewandowski, J. J., and Seifi, M., 2016, "Metal Additive Manufacturing: A Review of Mechanical Properties," *Annu. Rev. Mater. Res.*, **46**(1), pp. 151–186.
- [11] DebRoy, T., Wei, H. L., Zuback, J. S., Mukherjee, T., Elmer, J. W., Milewski, J. O., Beese, A. M., Wilson-Heid, A., De, A., and Zhang, W., 2018, "Additive Manufacturing of Metallic Components—Process, Structure and Properties," *Prog. Mater. Sci.*, **92**(3), pp. 112–224.
- [12] Foteinopoulos, P., Papacharalampopoulos, A., and Stavropoulos, P., 2018, "On Thermal Modeling of Additive Manufacturing Processes," *CIRP J. Manuf. Sci. Technol.*, **20**(1), pp. 66–83.
- [13] Sames, W. J., List, F., Pannala, S., Dehoff, R. R., and Babu, S. S., 2016, "The Metallurgy and Processing Science of Metal Additive Manufacturing," *Int. Mater. Rev.*, **61**(5), pp. 315–360.
- [14] Kruth, J. P., Froyen, L., Van Vaerenbergh, J., Mercelis, P., Rombouts, M., and Lauwers, B., 2004, "Selective Laser Melting of Iron-Based Powder," *J. Mater. Process. Technol.*, **149**(1), pp. 616–622.
- [15] Raghavan, N., Dehoff, R., Pannala, S., Simunovic, S., Kirka, M., Turner, J., Carlson, N., and Babu, S. S., 2016, "Numerical Modeling of Heat-Transfer and

- the Influence of Process Parameters on Tailoring the Grain Morphology of IN718 in Electron Beam Additive Manufacturing," *Acta Mater.*, **112**(11), pp. 303–314.
- [16] Everton, S. K., Hirsch, M., Stravroulakis, P., Leach, R. K., and Clare, A. T., 2016, "Review of In-Situ Process Monitoring and In-Situ Metrology for Metal Additive Manufacturing," *Mater. Des.*, **95**(7), pp. 431–445.
 - [17] Maskery, I., Aboulkhair, N. T., Corfield, M. R., Tuck, C., Clare, A. T., Leach, R. K., Wildman, R. D., Ashcroft, I. A., and Hague, R. J. M., 2016, "Quantification and Characterisation of Porosity in Selectively Laser Melted Al-Si10-Mg Using X-Ray Computed Tomography," *Mater. Charact.*, **111**(1), pp. 193–204.
 - [18] Hadadzadeh, A., Amirkhiz, B. S., Li, J., and Mohammadi, M., 2018, "Columnar to Equiaxed Transition During Direct Metal Laser Sintering of AlSi10Mg Alloy: Effect of Building Direction," *Addit. Manuf.*, **23**(5), pp. 121–131.
 - [19] Roberts, I. A., Wang, C., Esterlein, R., Stanford, M., and Mynors, D., 2009, "A Three-Dimensional Finite Element Analysis of the Temperature Field During Laser Melting of Metal Powders in Additive Layer Manufacturing," *Int. J. Mach. Tools Manuf.*, **49**(12–13), pp. 916–923.
 - [20] Markl, M., and Körner, C., 2016, "Multiscale Modeling of Powder Bed-Based Additive Manufacturing," *Annu. Rev. Mater. Res.*, **46**(1), pp. 93–123.
 - [21] King, W. E., Anderson, A. T., Ferencz, R., Hodge, N., Kamath, C., Khairallah, S. A., and Rubenchik, A. M., 2015, "Laser Powder Bed Fusion Additive Manufacturing of Metals: Physics, Computational, and Materials Challenges," *Appl. Phys. Rev.*, **2**(4), p. 041304.
 - [22] Khairallah, S. A., Anderson, A. T., Rubenchik, A., and King, W. E., 2016, "Laser Powder-Bed Fusion Additive Manufacturing: Physics of Complex Melt Flow and Formation Mechanisms of Pores, Spatter, and Denudation Zones," *Acta Mater.*, **108**(7), pp. 36–45.
 - [23] Bourell, D., Kruth, J. P., Leu, M., Levy, G., Rosen, D., Beese, A. M., and Clare, A., 2017, "Materials for Additive Manufacturing," *CIRP Ann.*, **66**(2), pp. 659–681.
 - [24] Seifi, M., Salem, A., Beuth, J., Harrysson, O., and Lewandowski, J. J., 2016, "Overview of Materials Qualification Needs for Metal Additive Manufacturing," *JOM*, **68**(3), pp. 747–764.
 - [25] O'Regan, P., Prickett, P., Setchi, R., Hankins, G., and Jones, N., 2016, "Metal Based Additive Layer Manufacturing: Variations, Correlations and Process Control," *Proc. Comput. Sci.*, **96**(19), pp. 216–224.
 - [26] Huang, Y., Leu, M., Mazumder, J., and Donmez, A., 2015, "Additive Manufacturing: Current State, Future Potential, Gaps and Needs, and Recommendations," *ASME J. Manuf. Sci. Eng.*, **137**(1), p. 014001.
 - [27] Huang, Y., and Leu, M., 2013, "Frontiers of Additive Manufacturing Research and Education—Report of NSF Additive Manufacturing Workshop," National Science Foundation, Arlington, VA.
 - [28] NIST, 2013, Measurement Science Roadmap for Metal-Based Additive Manufacturing - Report Prepared by Energetics Corporation," National Institute of Standards and Technology, Gaithersburg, MD.
 - [29] Mazumder, J., 2015, "Design for Metallic Additive Manufacturing Machine With Capability for 'Certify as You Build'," *Proc. CIRP*, **36**(10), pp. 187–192.
 - [30] Edgar, T., Davis, J., and Burka, M., 2015, "NSF Workshop on Research Needs in Advanced Sensors, Controls, Platforms, and Modeling (ASCPM) for Smart Manufacturing," National Science Foundation, Atlanta, GA.
 - [31] Simpson, T. W., Williams, C. B., and Hripko, M., 2017, "Preparing Industry for Additive Manufacturing and Its Applications: Summary & Recommendations From a National Science Foundation Workshop," *Addit. Manuf.*, **13**(1), pp. 166–178.
 - [32] Gu, H., Gong, H., Pal, D., Rafi, K., Starr, T., and Stucker, B., 2013, "Influences of Energy Density on Porosity and Microstructure of Selective Laser Melted 17-4PH Stainless Steel," Proceedings of the 2013 Solid Freeform Fabrication Symposium, University of Texas, Austin, Aug. 12–14, pp. 474–489.
 - [33] Gong, H., Rafi, K., Gu, H., Starr, T., and Stucker, B., 2014, "Analysis of Defect Generation in Ti-6Al-4V Parts Made Using Powder Bed Fusion Additive Manufacturing Processes," *Addit. Manuf.*, **1**(4–1), pp. 87–98.
 - [34] Gong, H., Rafi, K., Starr, T., and Stucker, B., 2012, "Effect of Defects on Fatigue Tests of As-Built Ti-6Al-4V Parts Fabricated by Selective Laser Melting," Proceedings of the Solid Freeform Fabrication Symposium, University of Texas, Austin, Aug. 6–8, pp. 499–506.
 - [35] Montazeri, M., Yavari, R., Rao, P., and Boulware, P., 2018, "In-Process Monitoring of Material Cross-Contamination Defects in Laser Powder Bed Fusion," *ASME J. Manuf. Sci. Eng.*, **140**(11), p. 111001.
 - [36] Montazeri, M., and Rao, P., 2018, "Sensor-Based Build Condition Monitoring in Laser Powder Bed Fusion Additive Manufacturing Process Using a Spectral Graph Theoretic Approach," *ASME J. Manuf. Sci. Eng.*, **140**(9), p. 091002.
 - [37] Fox, J. C., Moylan, S. P., and Lane, B. M., 2016, "Effect of Process Parameters on the Surface Roughness of Overhanging Structures in Laser Powder Bed Fusion Additive Manufacturing," *Proc. CIRP*, **45**(6), pp. 131–134.
 - [38] Strano, G., Hao, L., Everson, R., and Evans, K., 2013, "A New Approach to the Design and Optimisation of Support Structures in Additive Manufacturing," *Int. J. Adv. Manuf. Technol.*, **66**(9–12), pp. 1247–1254.
 - [39] Thomas, D., 2009, "The Development of Design Rules for Selective Laser Melting," Ph.D. Dissertation, University of Wales. <http://hdl.handle.net/10369/913>.
 - [40] Jamshidinia, M., and Kovacevic, R., 2015, "The Influence of Heat Accumulation on the Surface Roughness in Powder-Bed Additive Manufacturing," *Surf. Topogr.: Metrol. Prop.*, **3**(1), p. 014003.
 - [41] Denlinger, E. R., Irwin, J., and Michaleris, P., 2014, "Thermomechanical Modeling of Additive Manufacturing Large Parts," *ASME J. Manuf. Sci. Eng.*, **136**(6), p. 061007.
 - [42] Bandyopadhyay, A., and Traxel, K. D., 2018, "Invited Review Article: Metal-Additive Manufacturing—Modeling Strategies for Application-Optimized Designs," *Addit. Manuf.*, **22**(4), pp. 758–774.
 - [43] Denlinger, E. R., Gouge, M., and Michaleris, P., 2018, *Thermo-Mechanical Modeling of Additive Manufacturing*, Butterworth-Heinemann, London.
 - [44] Francois, M. M., Sun, A., King, W. E., Henson, N. J., Tourret, D., Bronkhorst, C. A., Carlson, N. N., Newman, C. K., Haut, T., Bakosi, J., Gibbs, J. W., Livescu, V., Vander Wiel, S. A., Clarke, A. J., Schraad, M. W., Blacker, T., Lim, H., Rodgers, T., Owen, S., Abdeljawad, F., Madison, J., Anderson, A. T., Fattebert, J. L., Ferencz, R. M., Hodge, N. E., Khairallah, S. A., and Walton, O., 2017, "Modeling of Additive Manufacturing Processes for Metals: Challenges and Opportunities," *Curr. Opin. Solid State Mater. Sci.*, **21**(4), pp. 198–206.
 - [45] Cheng, B., Shrestha, S., and Chou, Y. K., 2016, "Stress and Deformation Evaluations of Scanning Strategy Effect in Selective Laser Melting," *Proceedings of the ASME 2016 11th International Manufacturing Science and Engineering Conference*, Blacksburg, VA, June 27–30, p. V003T008A009.
 - [46] Williams, R. J., Davies, C. M., and Hooper, P. A., 2018, "A Pragmatic Part Scale Model for Residual Stress and Distortion Prediction in Powder Bed Fusion," *Addit. Manuf.*, **22**(4), pp. 416–425.
 - [47] Zeng, K., Pal, D., Gong, H. J., Patil, N., and Stucker, B., 2015, "Comparison of 3DSIM Thermal Modelling of Selective Laser Melting Using New Dynamic Meshing Method to ANSYS," *Mater. Sci. Technol.*, **31**(8), pp. 945–956.
 - [48] Luo, Z., and Zhao, Y., 2018, "A Survey of Finite Element Analysis of Temperature and Thermal Stress Fields in Powder Bed Fusion Additive Manufacturing," *Addit. Manuf.*, **21**(3), pp. 318–332.
 - [49] Michaleris, P., 2014, "Modeling Metal Deposition in Heat Transfer Analyses of Additive Manufacturing Processes," *Finite Elem. Anal. Des.*, **86**(9), pp. 51–60.
 - [50] Peng, H., Ghasri-Khouzani, M., Gong, S., Attardo, R., Ostiguy, P., Gatrell, B. A., Budzinski, J., Tomonto, C., Neidig, J., Shankar, M. R., Billo, R., Go, D. B., and Hoelzle, D., 2018, "Fast Prediction of Thermal Distortion in Metal Powder Bed Fusion Additive Manufacturing: Part 1, A Thermal Circuit Network Model," *Addit. Manuf.*, **22**, pp. 852–868.
 - [51] Ganeriwala, R., and Zohdi, T. I., 2014, "Multiphysics Modeling and Simulation of Selective Laser Sintering Manufacturing Processes," *Proc. CIRP*, **14**(2), pp. 299–304.
 - [52] Ganeriwala, R., and Zohdi, T. I., 2016, "A Coupled Discrete Element-Finite Difference Model of Selective Laser Sintering," *Granul. Matter*, **18**(2), p. 21.
 - [53] Solomon, J., 2015, "PDE Approaches to Graph Analysis," preprint arXiv:1505.00185.
 - [54] Belkin, M., Sun, J., and Wang, Y., 2008, "Discrete Laplace Operator on Meshed Surfaces," *Proceedings of the Twenty-Fourth Annual Symposium on Computational Geometry*, College Park, MD, June 9–11, pp. 278–287.
 - [55] Zhang, F., and Hancock, E. R., 2008, "Graph Spectral Image Smoothing Using the Heat Kernel," *Pattern Recognit.*, **41**(11), pp. 3328–3342.
 - [56] Silling, S. A., and Askari, E., 2005, "A Meshfree Method Based on the Peridynamic Model of Solid Mechanics," *Comput. Struct.*, **83**(17), pp. 1526–1535.
 - [57] Chen, Z., Niazi, S., Zhang, G., and Bobaru, F., 2017, "Peridynamic Functionally Graded and Porous Materials: Modeling Fracture and Damage," *Handbook of Nonlocal Continuum Mechanics for Materials and Structures*, G. Z. Voyiadjis, ed., Springer International Publishing, Cham, pp. 1–35.
 - [58] Sun, Y.-S., and Li, B.-W., 2010, "Spectral Collocation Method for Transient Conduction-Radiation Heat Transfer," *J. Thermophys. Heat Transf.*, **24**(4), pp. 823–832.
 - [59] Rahmati, A. R., and Niazi, S., 2012, "Simulation of Microflows Using the Lattice Boltzmann Method on Nonuniform Meshes," *Nanosci. Technol.*, **3**(1), pp. 77–97.
 - [60] Kondor, R. I., and Lafferty, J. D., 2002, "Diffusion Kernels on Graphs and Other Discrete Input Spaces," Proceedings of the 19th International Conference on Machine Learning., San Francisco, CA, July 8–12, pp. 315–322.
 - [61] Saito, N., 2013, "Tutorial: Laplacian Eigenfunctions—Foundations and Applications," University of California, Davis, Graduate University for Advanced Studies, National Institute of Fusion Science, Japan.
 - [62] Chung, F. R. K., 1997, *Spectral Graph Theory*, American Mathematical Society, Providence, RI.
 - [63] Bai, X., and Hancock, E. R., *Heat Kernels, Manifolds and Graph Embedding*, Springer, Berlin Heidelberg, pp. 198–206.
 - [64] Goldak, J. A., and Akhlaghi, M., 2005, "Computer Simulation of Welding Processes," *Computational Welding Mechanics*, pp. 16–69.
 - [65] Goldak, J., Chakravarti, A., and Bibby, M., 1984, "A New Finite Element Model for Welding Heat Sources," *Mettall. Trans. B*, **15**(2), pp. 299–305.
 - [66] Cole, K. D., Beck, J. V., Haji-Sheikh, A., and Litkouhi, B., 2010, *Heat Conduction Using Green's Functions*, CRC Press, Boca Raton, FL.
 - [67] Cole, K. D., 2018, "Parallelepiped with Insulated Boundaries and Piecewise Initial Condition" EXACT Analytical Conduction Toolbox, Oct. 18.
 - [68] Nunes, A., 1983, "An Extended Rosenthal Weld Model," *Weld. J.*, **62**(6), pp. 165s–170s.
 - [69] Karayagiz, K., Elwany, A., Tapia, G., Franco, B., Johnson, L., Ma, J., Karaman, I., and Arróyave, R., 2018, "Numerical and Experimental Analysis of Heat Distribution in the Laser Powder Bed Fusion of Ti-6Al-4V," *IISE Trans.*, **51**(2), pp. 136–152.
 - [70] Rubenchik, A., Wu, S., Mitchell, S., Golosker, I., LeBlanc, M., and Peterson, N., 2015, "Direct Measurements of Temperature-Dependent Laser Absorptivity of Metal Powders," *Appl. Opt.*, **54**(24), pp. 7230–7233.